High Q-factor measurements and prolonged Raman lasing

in microdroplets standing on a superhydrophobic surface

by

Mustafa Gündoğan

A Thesis Submitted to the

Graduate School of Engineering

in Partial Fulfillment of the Requirements for

the Degree of

Master of Science

in

Physics

Koç University

August 2010

Koç University

Graduate School of Sciences and Engineering

This is to certify that I have examined this copy of a master's thesis by

Mustafa Gündoğan

and have found that it is complete and satisfactory in all respects,
and that any and all revisions required by the final
examining committee have been made.

Committee Members:

_____

Alper Kiraz, Ph. D. (Advisor)

_____

Alphan Sennaroğlu, Ph. D.

_____

Özgür Birer, Ph. D.

Date: _____

ii

ABSTRACT

Optical microcavities are platforms in which the light-matter interactions are investigated and novel photonic and optoelectronic device concepts are introduced and tested. From the basic scientific point of view, they are important for quantum and nonlinear optical studies, whereas from a technological perspective, future computers and telecommunication components can benefit from microcavity based devices. The results of this thesis are presented in two parts; i) characterizing liquid microdroplets as optical microcavities and ii) sustainable microdroplet Raman laser, both with the help of recently demonstrated reversible photothermal tuning of a droplet.

High Quality factors (Q-factors) are essential for studies in especially quantum and nonlinear optics. Previous attempts of Q-factor measurements were limited by the resolution (0.07 nm) of the monochromator present in the laboratory which corresponds to a Q-factor of about 8100 around 650 nm. In the first part of the thesis, we made use of reversible photothermal tuning to overcome this limitation. When heated, certain amount of water evaporates, thus changes the equilibrium size of the microdroplet. In order to measure the Q-factor, we continuously change the power of the IR laser in very small steps, which enables tuning of the size of the microdroplet accordingly. WGMs of a dye-doped microdroplet are simultaneously excited by a probe laser and dye emission is monitored with an avalanche photo diode (APD). A peak is observed in the APD signal when the resonance condition is satisfied. Q-factors up to 10^5 are measured with this method. We achieved a resolution around 0.004 nm, which implies that we have the ability to tune the droplet's radius with a precision of $\leq 1\mathring{A}$.

In the second part of the thesis, we demonstrate sustained Raman lasing from NaCl-water microdroplets with time periods as long as 25 minutes. In principle, there is no upper limit and all the experiments were terminated after sufficient amount of data were gathered.

The technique we present relies on two lasers: a cw IR laser for photothermal tuning, and a pulsed green laser for size stabilization and excitation of the Raman band. It was previously shown that resonant heating of a droplet can lead to size stabilization due to size-dependent absorption. In this study, we combine this effect with photothermal tuning to sustain Raman lasing in long time scales. By photothermal tuning, the size of the droplet is tuned to a specific size in resonance with the green laser. From then on, resonant heating of the green laser leads to size stabilization, which eliminates the previously observed on-off behavior. However, long term fluctuation in the chamber still needs to be suppressed and it is compensated by slight manual adjustments of IR laser power after Raman lasing is detected.

ÖZET

Optik mikrokovuklar ışık-madde etkileşmelerinin incelendiği ve özgün fotonik ve optoelektronik cihaz konseptlerinin geliştirildiği ve test edildiği platformlardır. Temel bilim açısından bakıldığında, kuantum ve doğrusal olmayan optic alanında önemlidir. Teknolojik açıdan ise gelecekteki bilgisayar ve telekomünikasyon cihazları bu yapılardan istifade edebilir. Bu tezin sonuçları iki ana kısımda sunulmaktadır; i) sıvı mikrodamlacıkları optic mikrokovuk olarak karakterize etmek ve ii) sürdürülebilir mikrodamla Raman lazeri gösterimi. Her iki kısımda da yeni gösterilen damlacığın tersinebilir fototermal tarama tekniği kullanılmıştır.

Yüksek Kalite faktörleri (*Q-faktör*) özellikle kuantum ve doğrusal olmayan optik çalışmaları için önemlidir. Laboratuvarımızda önceki Q-faktör ölçüm denemeleri monokromatörün çözünürlüğü ile (0.07 nm) sınırlanmış olup, yaklaşık 650 nm civarında 8100 civarı bir Q-faktöre tekabül etmekteydi. Tezin ilk kısmında tersinebilir fototermal tarama tekniğini bu kısıtlamayı ortadan kaldırmak için kullandık. Q-faktörleri ölçmek için bu teknikle damlacığın boyu çok hassas bir biçimde sürekli olarak tarandı. Aynı zamanda boya molekülü katkılanmış olan bu damlacıklar Fısıldayan Galeri Kipleri (FGK) mavi lazer ile uyarıldı. Rezonans durumu sağlandığında tek foton detektöründe bir pik görüldü. Bu metodla 10^5 mertebesinde Q-faktörler ölçüldü. Damlacığın boyunu $\leq 1\overset{\circ}{A}$ hassasiyetle taradığımızı işaret eden 0.004 nm çözünürlük elde edildi.

Tezin ikinci kısmında ise NaCl-su damlacıklarından 25 dakikaya kadar sürdürülebilen Raman lazeri gösteriyoruz. Prensip olarak deneylerimizde üst zaman limiti yoktur ve bütün deneyler yeterli data toplandıktan sonra manuel olarak sonlandırılmıştır. Gösterdiğimiz teknik iki lazerle çalışmaktadır: fototermal tarama için sürekli dalga infrared (IR) lazer, ve boyut sabitlemesi ve Raman bandı uyarılması için darbeli yeşil pompa lazeri. Daha önce damlaların rezonans ısıtmasının boyuta bağlı soğurma nedeniyle boyut

sabitlemesine yol açacağı gösterilmişti. Bu çalışmada, bu tekniği fototermal tarama tekniği ile birleştirerek uzun surely Raman lazeri gösterimi için kullandık. Fototermal tarama ile damlacığın boyu yeşil lazer ile rezonansa yakın bir boya getirilir. Bu noktadan sonra ise yeşil lazerin rezonans ısıtması daha önce gözlemlenen açık-kapalı davranışını yokeden bir boyut sabitlemesini sağlar. Buna rağmen nem hücresindeki uzun sureli, yavaş dalgalanmaları elimine etmek için Raman lazeri çalışmaya başladıktan sonra IR lazerin gücü küçük manuel ayarlamalarla değiştirilmiştir.

ACKNOWLEDGEMENTS

I would like to thank my advisor Prof. Alper Kiraz for his friendly support, guidance and helps throughout the course of my master studies. I also want to thank him for providing me with the independence and the flexibility that I need to develop myself.

I would like to thank Profs. Alphan Sennaroğlu and Özgür Birer for their critical comments on the manuscript of this thesis, and also for being committee members.

I would like to thank Prof. Ali Serpengüzel for not only giving me a great insight into physics and particularly in optics through his memorable courses, but also for his academic and career related advices.

I greatly remember Profs. Ceyhun Bulutay, Özgür Oktel and Atilla Aydınlı of Bilkent and Prof. Ahmet Oral of Sabancı Universities for their support and encouragement in my undergraduate years.

I gratefully acknowledge the present and former members of our group, especially Dr. Michael Mestre, Yasin Karadağ and Mehdi Yavuz Yüce. It was great to work with these people.

Life at Koç would not have been this much joyful without the friends from nearly all the departments. I want to thank them all for all the good days that we spent together.

Finally above all, I am indebted to Manolya Ün and my family for their love and patience throughout the years.

TABLE OF CONTENTS

List of Figures

x

Nomenclature

θ_{inc}	angle of incidence
λ	wavelength
ω	angular frequency
$\boldsymbol{m}(\omega)$	complex refraction index of the dielectric material
x	size parameter
FWHM	full width at half maximum
WGM	whispering gallery mode
S_A	relative water humidity in the chamber
γ_A	activity coefficient of water
D_A	molecular diffusivity in the gas mixture
x_A	mole fraction of water
$P_A^0(T)$	vapor pressure at temperature
T_d, T_∞	temperatures at the air–microdroplet interface and in the chamber far from the microdroplet
V_m	molar specific volume
C_{PL}	molar heat capacity of the microdroplet mixture
k_{eff}	area average of the heat conductivities of the air and the substrate
P_{inc}	total power of the incident beam
$\tilde{Q}_{abs}$	ratio of the total power absorbed by the droplet to the total power of the incident beam
f_{PB}	correction factor due the existence of the surface
$\Delta\lambda_{max}$	magnitude of the maximum spectral drift observed for the maximum available infrared laser power
P_{IR}	infrared laser power
K_a	thermal conductivity of the surrounding air
f	fraction of the laser that is coupled to a WGM

Chapter 1

Introduction

1.1 Overview

Investigation of light-matter interactions at small scales has always been a hot topic in physics. From the discoveries of Raman [1] and Brillouin [2] scatterings in the beginning of the century to the current state-of-the-art cavity quantum electrodynamics (c-QED) experiments, scientists have always been interested in this topic. After the demonstration of the Purcell effect [3], importance of a cavity became apparent. Purcell effect is the enhancement of the rate of spontaneous emission of an ensemble of atoms when put in a resonance cavity. This enhancement means that the interaction time is prolonged since now there is more circulating power inside the cavity and, it is also essential to obtain radiation consisting of single wavelength or selecting a specific wavelength from a broadband radiation.

Different types of microcavities have been demonstrated so far. These include silica spheres [4], semiconductor disks [5], toroids [6], micropillars [7], photonic crystal defect cavities [8] and droplets [9, 10]. Each type of cavity has its own advantage. For example solid microcavities, especially silica sphere and torus cavities have the highest Q-factor among all, but they lack large tunability. Another example is that photonic crystal nanocavities have the smallest mode volume due to their small size, but the imperfections of fabrication processes put a limitation on their Q-factor. Liquid microdroplets, on the other hand, are easy to produce, are simple, and have large tunability. But their size is very sensitive to external fluctuations. This puts important limitations on the Q-factors observed from individual droplets.
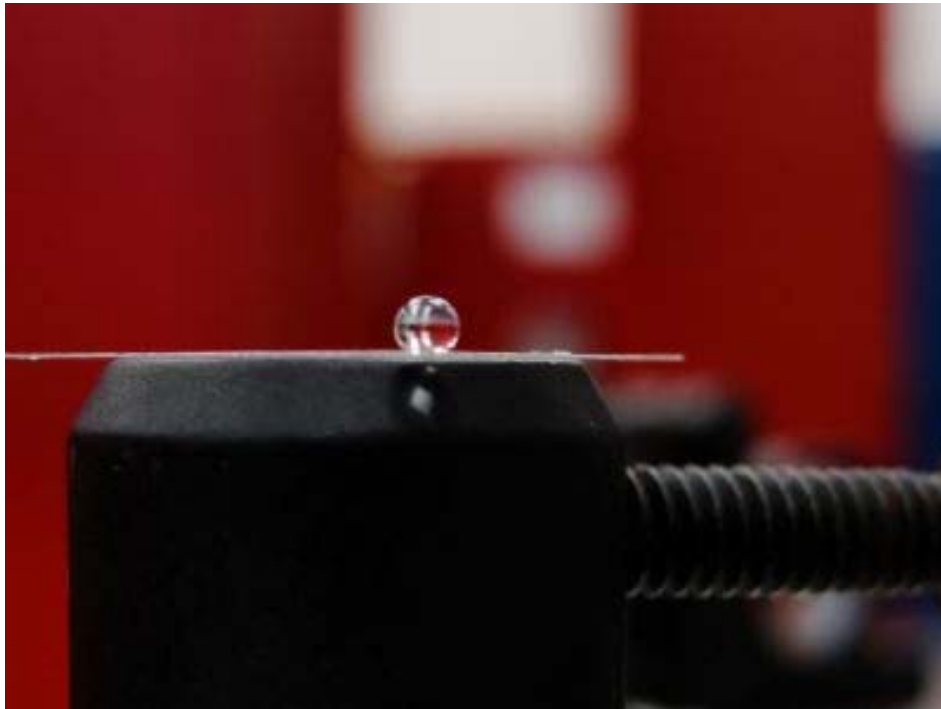
Figure 1.1. A millimeter-sized droplet standing on a superhydrophobic surface.

In this thesis, we investigate liquid microdroplets standing on a superhydrophobic surface as optical cavities. Our research group previously demonstrated for the first time that a droplet standing on a substrate exhibits characteristics of optical cavities – resonance modes, which for spherical and circular cavities called Whispering Gallery Modes (WGMs) [10]. After this demonstration, some of the numerous experiments that were done in our laboratory were to observe Raman lasing [11], to stabilize size with very high precision [12] and to reversibly tune [13] the resonance modes.

Figure 1.2. Red illuminated microdroplet under microscope. Reflection on the left is caused by the total internal reflection from the inner surface of the droplet.

In this thesis, we concentrate on, first, characterization of these cavities i.e. Q-factor measurements and, second, an application i.e. prolonging the duration of Raman lasing by size stabilization. Our study represents two characteristics of scientific research, which are basic science, and application oriented science. Previously observed Q-factors of microdroplets in our lab were limited by the resolution of the spectrometer to around ~8100. Lack of a tunable laser led us to measure the Q-factors with previously demonstrated reversible size tuning mechanism. We measured Q-factors as high as 10^5, at least 10 times larger than the previous measurements. We later verified our results after acquiring a tunable laser. We then made use of the size stabilization technique to eliminate the previously observed on-off behavior in Raman lasing in microdroplets. We observed

lasing durations as high as 25 minutes, which is 1000 times longer than the previous studies.

1.2 Outline of the thesis

Chapter 1 begins with the general introduction to the subject and proceeds with the description of experimental techniques that are used in the thesis.

Chapter 2 summarizes the mathematical formulation of WGM of spherical dielectric resonators. Detailed description of the methods, (i) photothermal tuning and (ii) size stabilization are also included.

In Chapter 3, we present results of our Q-factor measurements obtained by photothermal tuning technique and by the use of the tunable laser.

Chapter 4 presents prolonged Raman lasing experiments, and it is followed by Chapter 5, in which we briefly summarize all the findings presented in this thesis.

1.3 Experimental setup and techniques

Superhydrophobic surfaces were prepared by spin coating the glass slides by 50 mg/ml ethanol dispersion of commercially available hydrophobically coated silica nanoparticles (Evonik, Aeroxide ® LE1) at 2000 rpm for 1 min. After coating, glass slides were post-baked at 80°C for around one hour for evaporation of remaining ethanol. NaCl-water solution is then sprayed onto the slide by an ultrasonic nebulizer. Average sizes of the resulting droplets are around a few micrometers to a few tens of micrometers. Contact angles of millimeter-sized droplets are measured to be $> 160°$.

We used different types of lasers for different purposes throughout our studies. We used Crystalaser cw infrared (IR) laser operating at 1064 nm with a maximum power of ~0.3 W. It is focused to the center of droplets for local heating in Q-factor measurements by photothermal tuning technique. It is however focused to the rim of the droplet for size

locking while measuring the Q-factor with the tunable laser. Tunable external cavity diode laser (New Focus TLB-6304) has a cw output and operates between 632 nm and 637.5 nm with two scanning modes. The resolution of the course scan is 0.02 nm. Fine scan range is only 0.11 nm (80 GHz). For exciting the WGMs for Q-factor measurements by photothermal tuning technique, a cw blue argon-ion laser (Cyonics Uniphase 2201-10SLSC) operating at 488 nm is used. Lastly, we used a frequency-doubled Q switched pulsed laser operating at 532 nm for pumping the Raman gain medium in the sustained Raman lasing experiments. The laser is located in the Laser Research Laboratory and the beam is transferred to our laboratory with a multi-mode optical fibre. Average power at the output of the optical fiber was measured to be around 60-70 mW.

The main experimental technique we use in Q-factor measurements is fluorescence excitation of dye molecules in microdroplets. Droplets are doped with fluorescent dye molecules which have absorption profiles large enough to cover the specific wavelengths of excitation laser. They have also large emission bandwidths which contain several WGMs. We used Rhodamine B as the molecule since the absorption profile fits well for excitation with a blue laser. However, on the other hand, we used Rhodamine 700 in experiments that involve the tunable laser.

We made the detection by means of either a ½ m monochromator or an avalanche photodiode (APD). The grating has 1200 grooves/mm, which yields a resolution around 0.07 nm around 590 nm. A CCD camera (Acton PIXIS 100) was used to record spectra.

Chapter 2

Whispering Gallery Modes and Photothermal Tuning of NaCl – Water Microdropelts

2.1 Whispering Gallery Modes

Light can be trapped inside a resonator by total internal reflection (TIR) if the resonance condition is satisfied. In its simplest form, for a spherical or a circular resonator this means the circumference of the resonator should be multiple times the wavelength of the light i.e. $2\pi r = n\lambda$. This simple relation may provide qualitative ideas but it is far from being convenient. In order to understand these resonance modes clearly, one needs to treat them with the electromagnetic theory.

In case of spherical or circular cavities, optical resonance modes are called either Morphology Dependent Resonances (MDRs) or Whispering Gallery Modes (WGMs). In this thesis we adopt the latter convention since it has been used in the relatively recent literature. In this section, we will review the mathematical formulation of resonance modes and provide quantitative analysis. We will mostly follow treatments of Refs. 14 and 15.

TIR is observed if the angle of incidence θ_{inc}, is greater than or equal to the critical angle θ_c, which is equal to $arcsin(1/\boldsymbol{m}(\omega))$, where $\boldsymbol{m}(\omega)$ is the complex angular frequency (ω) dependent refraction index of the dielectric material. If $2\pi r \gg \lambda$, that is $\theta_{inc} \approx 90°$, the path length can be approximated as the circumference of the circle. This constraint yields bounds lower and upper bounds for resonance wavelengths as;

$$\frac{2\pi r}{\lambda} \leq n \leq \frac{2\pi r \boldsymbol{m}(\omega)}{\lambda} \qquad (2.1)$$

where, n is a positive integer. Introducing the dimensionless size parameter $x = 2\pi r/\lambda$, resonance condition now becomes as $x \leq n \leq \boldsymbol{m}(\omega)x$. We need to solve Maxwell's equations with appropriate boundary conditions to have an understanding of the interaction between an electromagnetic wave and a dielectric sphere. If we assume a presence of sinusoidally varying EM wave (e.g. laser illumination), we write;

$$\mathbf{E}(r, \theta, \varphi; t) = \mathbf{E}(r, \theta, \varphi)e^{i\omega t} \tag{2.2}$$

$$\mathbf{H}(r, \theta, \varphi; t) = \mathbf{H}(r, \theta, \varphi)e^{i\omega t} \tag{2.3}$$

$$\dot{\mathbf{E}} = i\omega\mathbf{E} \tag{2.4}$$

$$\dot{\mathbf{H}} = i\omega\mathbf{H} \tag{2.5}$$

Curls of **E** and **H** are expressed as,

$$\nabla \times \mathbf{E} = -i\omega\mu_0\mathbf{H} \tag{2.6}$$

$$\nabla \times \mathbf{H} = -i\omega\epsilon_r\epsilon_0\mathbf{E} \tag{2.7}$$

Curl of (2.6) yields

$$\nabla \times (\nabla \times \mathbf{E}) = -i\omega\mu_0(\nabla \times \mathbf{H}) \tag{2.8}$$

left hand side may be rearranged by using a vector identity,

$$\nabla(\nabla \cdot E) - \nabla^2\mathbf{E} = -i\omega\mu_0(\nabla \times \mathbf{H}) \tag{2.9}$$

Using (2.7) and $\nabla \cdot \mathbf{E} = 0$ would finally give,

$$(\nabla^2 + \mu_0\epsilon_r\epsilon_0\omega^2)\mathbf{E} = 0 \tag{2.10}$$

Similar expression for **H** is also obtained as,

$$(\nabla^2 + \mu_0\epsilon_r\epsilon_0\omega^2)\mathbf{H} = 0 \tag{2.11}$$

There are two types of resonance modes transverse electric (TE) and transverse magnetic (TM) modes. Since they behave similarly, we will proceed for TE modes which satisfy the

equation $\mathbf{r} \cdot \mathbf{E} = 0$. Electric field can be decomposed into a vector and a scalar component as $\mathbf{E} = r \times \nabla\psi$. The scalar component should satisfy the Helmholtz equation; $(\nabla^2 + k^2)\psi = 0$, where $k^2 = \mu_0 \epsilon_r \epsilon_0 \omega^2$. Solution to this equation is obtained as,

$$\Psi(r, \theta, \varphi) = \frac{A}{\sqrt{r}} J_{n+1/2}(kr) P_n^m(\cos\theta)\cos m\varphi \tag{2.12}$$

where A is constant, $J_{n+1/2}$ is Bessel and $P_n^m(\cos\theta)$ is associated Legendré polynomials. If we put this into Helmholtz equation, three components of the electric field are found as [14],

$$E_r = 0 \tag{2.13}$$

$$E_\theta = \frac{Am}{\sqrt{r}\sin\theta} J_{n+1/2}(kr) P_n^m(\cos\theta)\sin m\theta \tag{2.14}$$

$$E_\varphi = \frac{A}{\sqrt{r}} J_{n+1/2}(kr) \frac{d}{d\theta}\{P_n^m(\cos\theta)\}\cos m\theta \tag{2.15}$$

And the characteristic equation for TE modes is given by [15],

$$\mathbf{m}(\omega) \frac{\psi_n'(\mathbf{m}(\omega)x)}{\psi_n(\mathbf{m}(\omega)x)} - \frac{\xi_n'(x)}{\xi(x)} = 0 \tag{2.16}$$

where $x = ka = 2\pi a/\lambda$ is the dimensionless size parameter, and ψ_n and $\xi(x)$ are Riccati-Bessel and Riccati-Hankel functions, respectively. l modes are obtained from the solution of the characteristic equation for each n mode. If n and $\mathbf{m}(\omega)$ are fixed the first two solutions are called $l = 1$ and $l = 2$ modes and so on. As mentioned in the beginning of this chapter, leakage loss cannot be explained by the ray picture of WGMs. At this point, we should note that even if there is no absorption loss, i.e. $\text{Im}(\boldsymbol{m}(\omega)) = 0$, solutions to the characteristic equation are complex resonance size parameters x_a. The real part of x_a is the position of the resonance mode whereas the imaginary part is related to the leakage loss

mode out of the dielectric cavity. More specifically these quantities are related to the *quality factor, Q,* through the following relation

$$Q = \frac{\text{Re}(x_a)}{\text{Im}(x_a)} = \frac{\omega_a}{\Delta\omega_a} = \omega_a\tau \qquad (2.17)$$

where, $\omega_a = c\text{Re}(x_a)/a$ is the resonance frequency, $\Delta\omega_a$ is the FWHM of the resonance and τ is the lifetime of the mode. Q-factors as high as 10^{100} are expected if we only take leakage loss into account. However, absorption, surface roughness and inhomogeneities put a lower limit around 10^{10}-10^{11} [16].
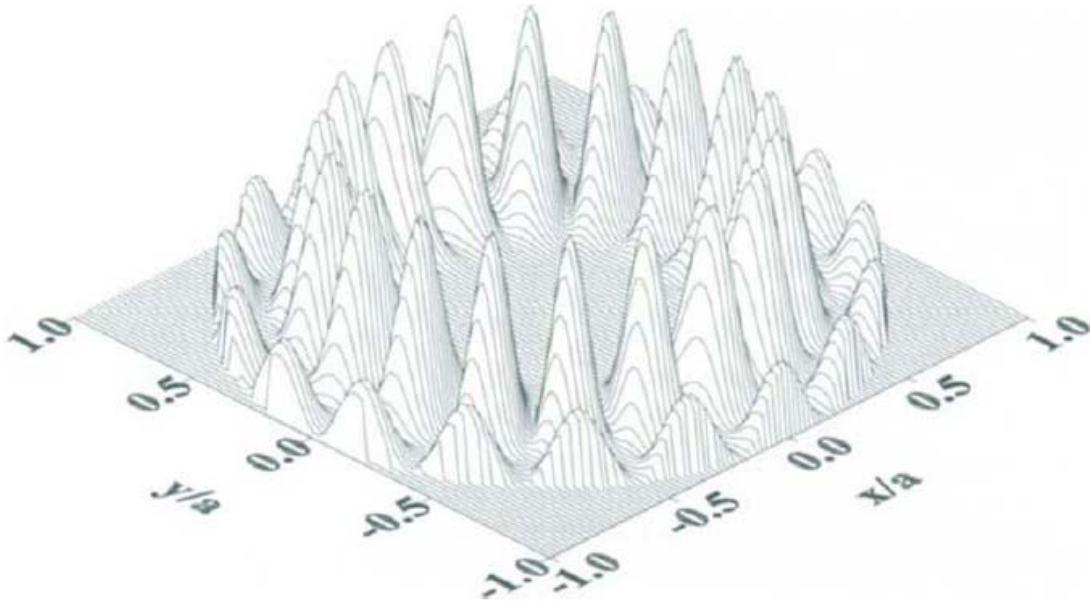
Figure 2.1 Intensity distribution of the circulating TE mode with $n = 9$ and $l = 2$. a is the radius [15].

n and l modes are obtained from equation 2.15. Figure 2.1 depicts the physical meaning of these numbers. Additionally, in perfect spheres there are $2n + 1$ number of modes

having the same *n* and *l* number. These modes are called *azimuthal modes* and they are degenerate since the radius of the sphere is constant in all different planes. This is illustrated in Figure 2.2.
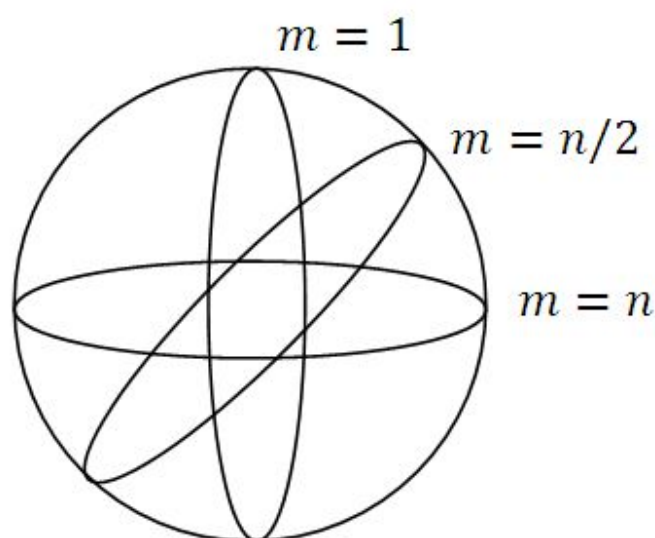
Figure 2.2: Azimuthal modes of a dielectric sphere.

2.2 Reversible Photothermal Tuning of a NaCl-Water Microdroplet

In this section we will summarize the findings of Kiraz et. al [13] and Karadag et. al [17] on the reversible photothermal tuning of droplet size. In these studies, it is shown that the size of a binary-compound droplet can be changed reversibly by local heating. Heating is realized by infrared (IR) laser illumination. Upon heating certain amount of water evaporates and thus the size of the droplet shrinks until a new equilibrium between the humidity of the ambient atmosphere and the droplet's vapor pressure is established. The

other compound should be volatile, i.e., the amount should be constant while the amount of water is changed during the process. Since droplets are contained in a sealed humidity chamber, the range of reversibility can be adjusted. It is found that, contrary to the common sense, tunability increases as the humidity of the chamber increases. Simple lumped system formulation describes the time evolution of the amount of water in the droplet,

$$\frac{dN_A}{dt} = -4\pi a f_{PB} D_A \frac{P_A^0(T_\infty)}{R T_\infty} (\gamma_A x_A \phi_A - S_A) \qquad (2.18)$$

where

$$\phi_A = \left(\frac{T_\infty}{T_d}\right) \frac{P_A^0(T_d)}{P_A^0(T_\infty)} \qquad (2.19)$$

Temperature change is given by,

$$\frac{dT_d}{dt} = \frac{\Delta H_{vap,A}}{N C_{PL}} \frac{dN_A}{dt} - \frac{3 k_{eff} V_m}{a^2 C_{PL}} + \frac{\tilde{Q}_{abs} P_{inc}}{N C_{PL}} \qquad (2.20)$$

where the first term is the temperature change due to the evaporation of water , second term is due the conductive cooling and the last term is the temperature change induced by the absorption of IR laser. In above equations S_A is the relative water humidity in the chamber, γ_A is the activity coefficient of water, and determines the vapor pressure of the droplet. D_A is the molecular diffusivity in the gas mixture, x_A is the mole fraction of water, R is the universal gas constant, $P_A^0(T)$ is the vapor pressure at temperature T, and T_d and T_∞ are the temperatures at the air–microdroplet interface and in the chamber far from the microdroplet, V_m is the molar specific volume, C_{PL} is the molar heat capacity of the microdroplet mixture, k_{eff} is the area average of the heat conductivities of the air and the substrate, and $\tilde{Q}_{abs}$ is the ratio of the total power absorbed by the droplet to the total power of the incident beam (P_{inc}) respectively. Finally, f_{PB} is the correction factor due the

existence of the surface, which is calculated (assuming a contact angle of 160°) by using Picknett and Bexon equation:

$$f_{PB} = \frac{1}{2}\begin{cases} 0.6366\theta + 0.09591\theta^2 - 0.06144\theta^3 & 0° \leq \theta < 10° \\ 0.000008957 + 0.6333\theta + 0.116\theta^2 - 0.08878\theta^3 + 0.01033\theta^4 & 10° \leq \theta < 180° \end{cases} \quad (2.21)$$

Details of $\tilde{Q}_{abs}$ calculation is given in Ref [18]. The radius change, thus the shift of spectral position of WGM is calculated from this model. It is found that this change varies linearly with changing IR laser power. The computer code used for solving this system is provided in Appendix A. Figure 2.4 shows this linear dependence. We verified this curve in our Q-factor measurement experiments as discussed in Chapter 3 where it is called the calibration curve.

Figure 2.3 shows the behaviour of $\tilde{Q}_{abs}$ for two different cases; laser illumination from the center (Fig. 2.3a) and from the rim (Fig 2.3b) of the droplet. Figure 2.3b shows that if the droplet is illimunated from the rim, due to the presence of WGMs, absorption has huge values and exhibit peaks at spectral positions corresponding to WGMs. This size-dependent absorption can lead to size stabilization. If the size of the droplet is higher than a specific value corresponding to a WGM, one has to increase the laser power to move towards the resonance (blue line in the inset) since the droplet size gets smaller as the laser power increases. But in the same time, resonant absorption also gets higher. So the droplet size passes the resonant size too quickly. But on the hand, if we start with a droplet radius which is smaller than the position of the specific resonance peak, the laser power has to be decreased to move towards (red line in the inset) the resonance. In the mean time, absorption heating gets higher, and at some point these decreasing and increasing heatings would compensate each other and a stable operation point is there established.
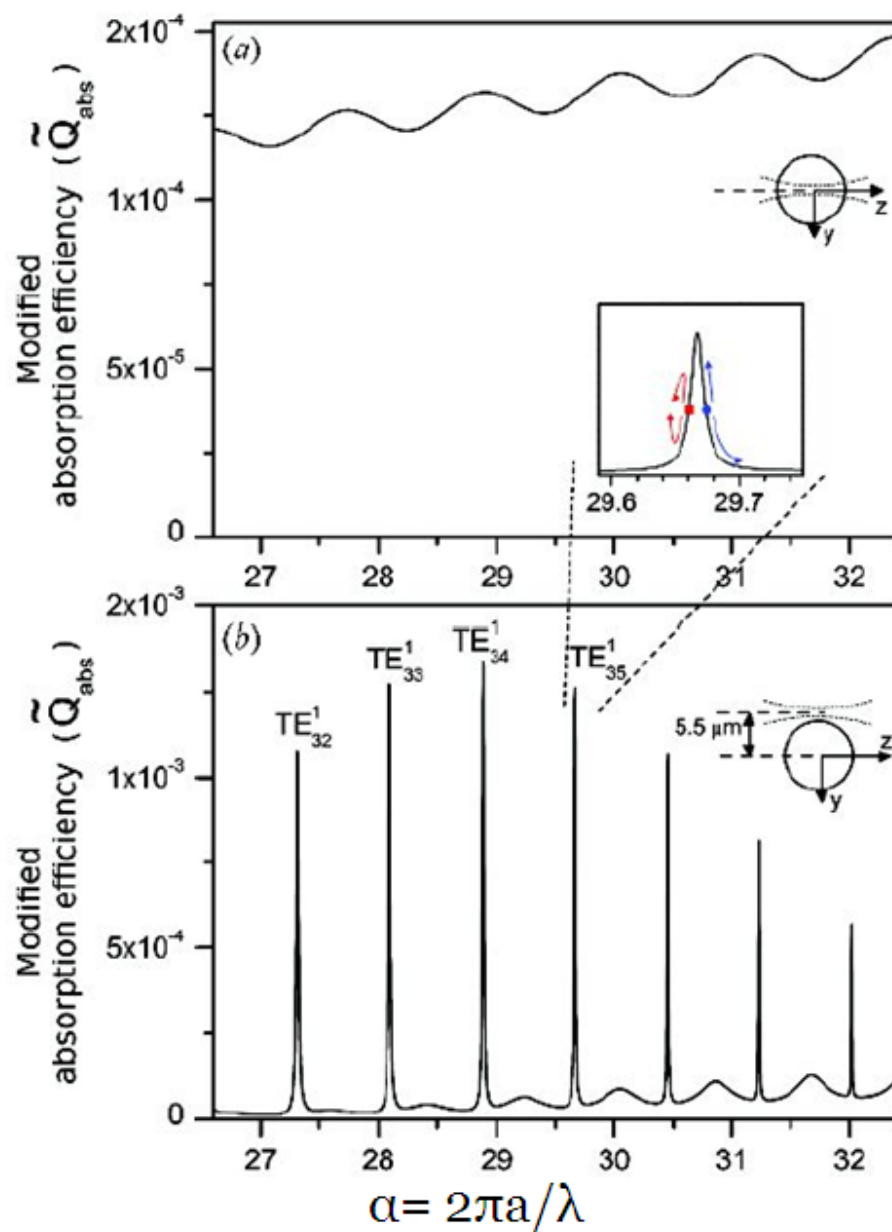
Figure 2.3: Behavior of the absorption efficiency ($\tilde{Q}_{abs}$) with respect to size for illumination from the center (a) and from the rim (b). Inset shows the self-stable operation.
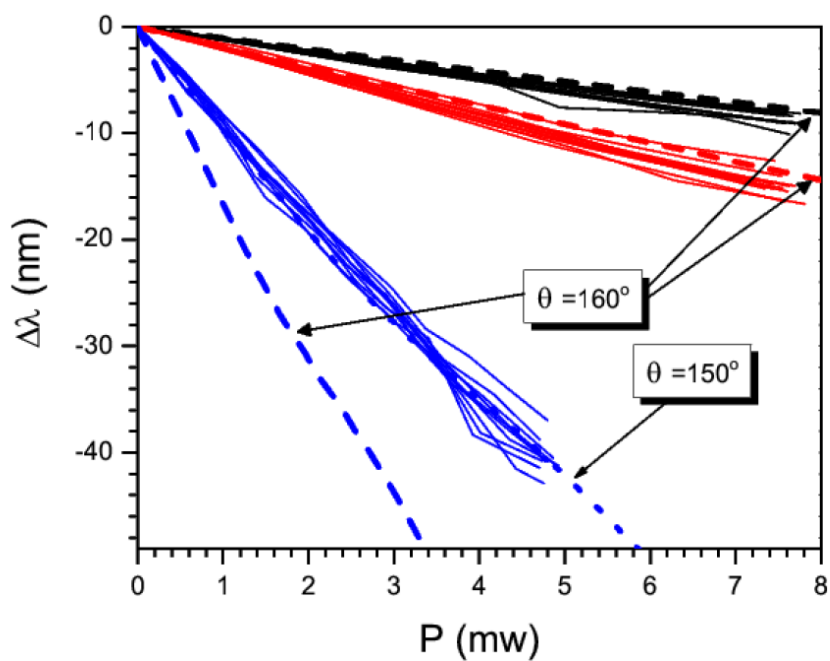
Figure 2.4: Experimental (solid) and computational (dashed) spectral drift of WGMs with different relative humidities (0.7530, 0.8434, 0.9730, respectively). Droplet radii are in the range of 7 − 10 μm, whereas the computation is done for a 7 μm droplet [18].

Chapter 3

Direct measurement of high Q-factors in individual salt-water microdroplets by photothermal spectroscopy

3.1 Introduction

High quality optical microcavities enable optical fields to strongly interact with embedded dipolar emitters or with mechanical degrees of freedom [19]. Absolute spectral positions of their high quality optical resonances are also very sensitive to environmental changes. These make high quality optical microcavities ideally suited for applications in cavity quantum electrodynamics, cavity optomechanics [20], and label-free biological sensing [21–23].

Among different high quality optical microcavities such as micropillars, microdisks, or photonic crystal defect cavities, microspheres and microtoroids excel due to the ultrahigh quality of their optical resonances [19]. Experiments using tunable lasers revealed quality factors (Q-factors) in the range between $10^8 - 10^{10}$ in these structures [16, 24, 25]. Liquid microdroplets are alternative optical microcavities which can host ultrahigh quality whispering gallery modes (WGMs) owing to their ideally spherical geometry and smooth surface [15, 26]. At visible wavelengths, Q-factors limited to $\sim 10^8$ mainly by material absorption are predicted for the first order WGMs of water microdroplets with a size parameter ($\alpha = 2\pi a/\lambda$, a and λ being the radius and wavelength) larger than ~ 60 [27]. Despite the predictions, direct Q-factor measurements based on the photon lifetime of elastically scattered light from individual microdroplets located in a linear stream revealed

Q-factors up to 5×10^5 [28]. Energy transfer experiments also revealed Q-factors of $\sim 5 \times 10^6$ for the WGMs of single electrodynamically levitated glycerol microdroplets [29].

Deformability is the critical advantage of liquid microdroplets over other solid optical microcavities. This however comes at the cost of the difficulty in stabilizing the position and size of individual liquid microdroplets. In the work we present here, the former challenge is overcome by the use of a superhydrophobic surface. This experimental configuration is easy to implement and preserves the spherical shape of the microdroplets while ultimately stabilizing their position. In contrast to other position stabilization techniques, i.e. electrodynamic levitation [30], optical levitation [31] or optical tweezing [32], liquid microdroplets do not perform any residual motion around their stable position while standing on a superhydrophobic surface. In this work, size stabilization is achieved by the addition of salt into water microdroplets that are kept in a chamber with fixed relative water humidity. Sizes of individual salt-water microdroplets are further controlled precisely and reversibly using the technique of photothermal tuning that we have recently demonstrated [13, 33]. Photothermal tuning relies on heating a salt-water microdroplet using an infrared laser focused at its center, the stable humidity of the chamber enabling it to reach an equilibrium size for arbitrary laser power values.

In this chapter, we report the measurement of the Q-factors of the WGMs observed at the absorption of an 488 nm probe laser focused to a microdroplet's rim. Measurements are performed by recording the fluorescence intensity from an individual dye-doped NaCl-water microdroplet as its size is scanned very precisely using photothermal tuning. The method presented here is therefore very similar to fluorescence (or photoluminescence) excitation spectroscopy [34], the only difference being the tuning of the microcavity resonance frequencies instead of that of the probe laser. The method is also analogous to the observation of resonances with a fixed-frequency probe while scanning the size of a Fabry-Perot resonator using a piezoelectric actuator. We present the measurement of Q-

factors up to $\sim 10^5$ for azimuthally degenerate WGMs. Compared to the spectral resolution obtained with a monochromator [10]; this corresponds to an improvement by almost one order of magnitude.

3.2 Experimental Setup

Our experimental setup probes WGMs of individual Rhodamine B-doped micrometer-sized NaCl-water droplets. The microdroplets are standing on a superhydrophobic surface and kept in a sealed humidity chamber. An infrared laser is used for controlled heating of the microdroplets, and a blue Argon-ion laser excites the Rhodamine-B dye molecules. A microscope in the inverted geometry is at the center of the setup: the superhydrophobic surface is placed at the focus of the objective, which enables visual selection of the microdroplet to be analyzed, focusing of the lasers onto the microdroplet, and collecting fluorescence light emitted by the dye molecules. An avalanche photodiode (APD) counts fluorescence photons as the infrared laser power is scanned using a motorized half-waveplate polarizer combination, recording a photothermal spectrum from the microdroplet. A monochromator also enables the recording of fluorescence spectra where WGMs are observed with a resolution lower than that of the photothermal spectra.

Superhydrophobic surfaces are prepared by spin coating a cover glass with 50 mg/mL ethanol dispersion of hydrophobically coated silica nanoparticles (Evonik Aeroxide® LE1). Microdroplets are sprayed on the surface by an ultrasonic nebulizer from a 5 M NaCl solution doped with $1 - 2$ μM Rhodamine B. After the microdroplets are generated, the cover glass is attached hermetically to the bottom of a humidity chamber whose relative water humidity is fixed to 84.34 % with a saturated KCl-water solution. Such a chamber enables to keep the microdroplets in very stable humidity and pressure conditions. The

chamber-surface ensemble is placed onto the microscope sample holder and left undisturbed for several hours to allow the microdroplets to reach their equilibrium sizes.

The experimental setup is shown in Figure 1. A solid state infrared cw laser (λ=1064 nm), linearly polarized at its output, is used for photothermal tuning of the microdroplets. A half-waveplate is mounted on a rotation stage linked with a timing belt to a computer-controlled rotational stepper motor with 6600 steps per revolution.

A polarizing beam splitter cube is placed on the beam path behind the waveplate; its undeflected output is sent to the sample while its deflected output is directed to a powermeter that indirectly measures the infrared laser power received by the sample. With this system, it is possible to change the infrared laser beam power from maximum to minimum (as allowed by the efficiency of the polarizer) in 1650 steps following a cosine curve. In the experiments reported here, a maximum infrared laser power of 625 μW at the focus of the microscope objective has been chosen as a compromise between resolution and tuning range.

An Argon-ion laser (λ_p = 488 nm, Cyonics Uniphase 2201-10SLSC) with a measured linewidth of 0.8 GHz is used as a probe to excite the Rhodamine B molecules in the microdroplet. It is important to note that for these experiments the probe laser linewidth needs to be smaller than the spectral resolution achieved in photothermal spectroscopy ($\sim$ 0.004 nm, corresponding to 5 GHz at 488 nm). The Argon-ion laser used in the experiments satisfies this criterion. Removable neutral density filters (optical density $\geq$ 2) are used to keep the Argon-ion laser power to a low level when recording a photothermal spectrum, in order not to saturate the APD as well as to minimize photobleaching of the Rhodamine B molecules. Typical Argon-ion laser powers of 0.2 μW and 95 μW at the focus of the microscope objective are used when recording photothermal spectra and conventional fluorescence spectra, respectively. The probe beam is dilated by a telescope to
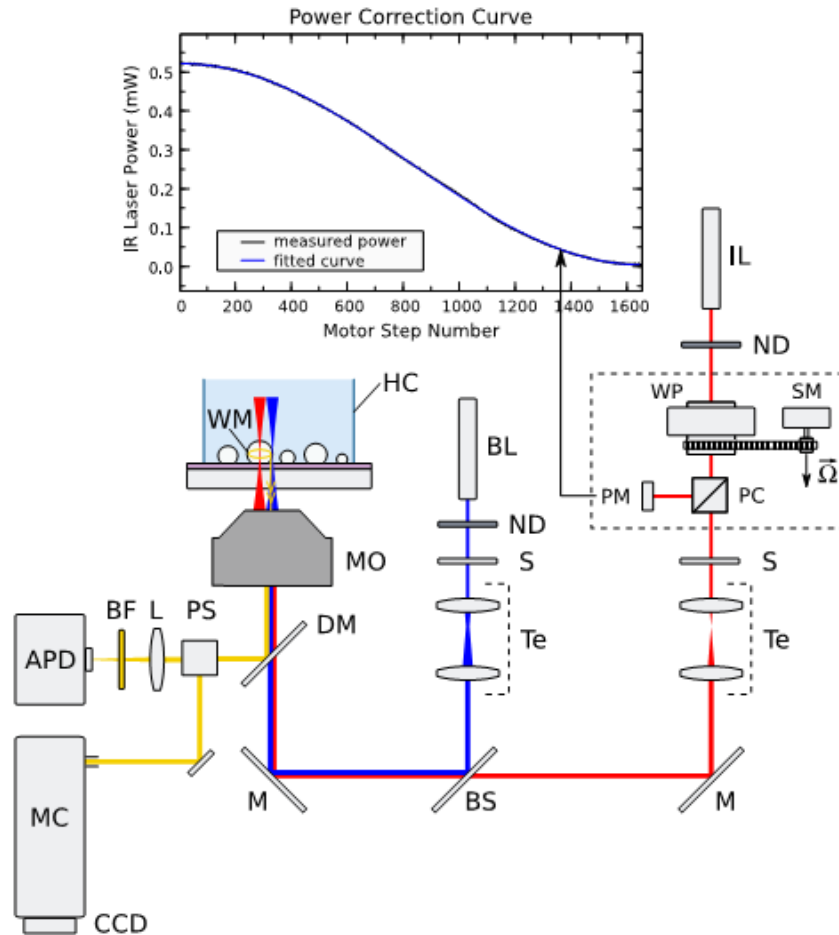
Figure 3.1: Optical setup. From lasers to sample; IL: infrared laser, ND: metallic neutral density filters, WP: ball bearing-mounted waveplate, SM: stepper motor with speed reducer, PC: polarizing cube, PM: powermeter, BL: blue Argon-ion laser, S: electromechanical shutter, Te: telescope, M: mirror, BS: beam splitter, DM: dichroic mirror, MO: microscope objective, HC: humidity chamber (partially drawn), WM: salt-water microdroplet, PS: microscope output port selector, L:focusing lens, BF: bandpass orange filters, APD: avalanche photodiode, MC: monochromator, CCD: spectrometer imaging sensor. Inset shows the motor step/optical power correction curve for a half period as measured directly by the powermeter.

optimize the waist size at the objective focus. Both the probe beam and the infrared beam are combined on a beam splitter and enter through the input port of the inverted microscope. They are focused by a high numerical aperture microscope objective (NA=1.4,

60x oil) onto the selected microdroplet resting on the superhydrophobic surface inside the humidity chamber. The blue (probe) beam is focused at the rim of the microdroplet to excite WGM resonances efficiently at 488 nm, while the infrared (heating) beam is directed towards the center of the microdroplet in order to heat it without exciting resonances at the infrared wavelength.

Rhodamine B fluorescence is collected by the same microscope objective, and sent either to the APD to record photothermal spectra, or to the monochromator to record conventional spectra, according to the output port selected on the microscope. The spectrometer used to record conventional fluorescence spectra consists of a 50 cm monochromator (resolution 0.07 nm at around 590 nm with a 1200 grooves/mm grating) and a CCD camera. The APD is equipped with a combination of two bandpass filters (HQ 605/40 and HQ 607/67) in order to restrict it to the fluorescence photons emitted by Rhodamine B molecules. A collecting lens focuses the light onto the active area of the APD to maximize the collected signal. A photothermal spectrum is recorded by integrating photon counts for each stepper motor position, corresponding to different infrared laser powers. At each step, the integration time (typically 100 ms to 500 ms) is followed by a delay time that is measured to be 16 ms. The powermeter placed at the deflected output of the polarizing beam splitter is used to measure the infrared laser power for different step values. Fluctuations in the powermeter readings are corrected by fitting the relationship between the stepper motor position and the powermeter readings to a sinusoidal function for each photothermal spectrum. The fitted curve provides both the total infrared laser power and the corrected infrared laser powers that correspond to each stepper motor position. The inset of Fig. 3.1 provides an example from one experiment of such a fitted power curve and the associated powermeter readings.

3.3 Description of the Photothermal Spectroscopy Technique

Scanning Fabry-Perot interferometers are equipped with a piezoelectric actuator onto which one of the two mirrors is mounted. When the voltage applied to the actuator is ramped, the cavity length is finely changed. By measuring the transmission of a fixed frequency incident laser beam through the Fabry-Perot cavity, the cavity resonances are observed. The photothermal spectroscopy method that we introduce here works in an analogous way; it relies on the ability to control finely and reversibly the evaporation/condensation of salt-water microdroplets in a sealed humidity chamber. By focusing an infrared laser beam onto the center of an individual microdroplet, its size is photothermally tuned in a reversible way. The amount of photothermal tuning is determined by the specific salt in the microdroplet and the relative water humidity of the chamber [10, 18]. Just like in the Fabry-Perot case, this size change leads to a shift in the resonance frequencies. A photothermal spectrum is then obtained by integrating photon counts from the APD that records the light emitted by the microdroplet as the intensity of the infrared laser is changed step by step. While the APD monitors light at around the fluorescence wavelength ($\lambda_f \simeq 590$ nm in this case for Rhodamine B), the intensity of the recorded signal is in fact proportional to the absorption of the probe laser ($\lambda_p = 488$ nm) by dye molecules in the microdroplet. This makes our technique similar to the well-known fluorescence (or photoluminescence) excitation spectroscopy [34].

Our goal is to observe narrow resonances, a low value for the total infrared laser power (625 μW at the focus of the microscope objective for the results presented here) is used to provide a good tuning resolution while keeping a comfortable tuning range. In order for the measurements to be meaningful, a calibration has to be performed for the relative wavelength shift at different values of the infrared laser power. The shape of such a calibration curve is linear (Figure 3.4) and we limit this calibration to a few power values.

For each of IR laser power values, a spectrum is recorded with the monochromator at the Rhodamine B fluorescence peak wavelength ($\lambda_f \simeq 590$ nm), and the wavelength drift of the WGMs is plotted. Figure 3.2 shows the calibration curves obtained on the same day from four different microdroplets with diameters ranging from 9 to 15 µm. As expected from the results of references [10, 18], microdroplets with different diameters located in the same environment

exhibit little differences in their photothermal tuning curves shown in Fig. 3.2.
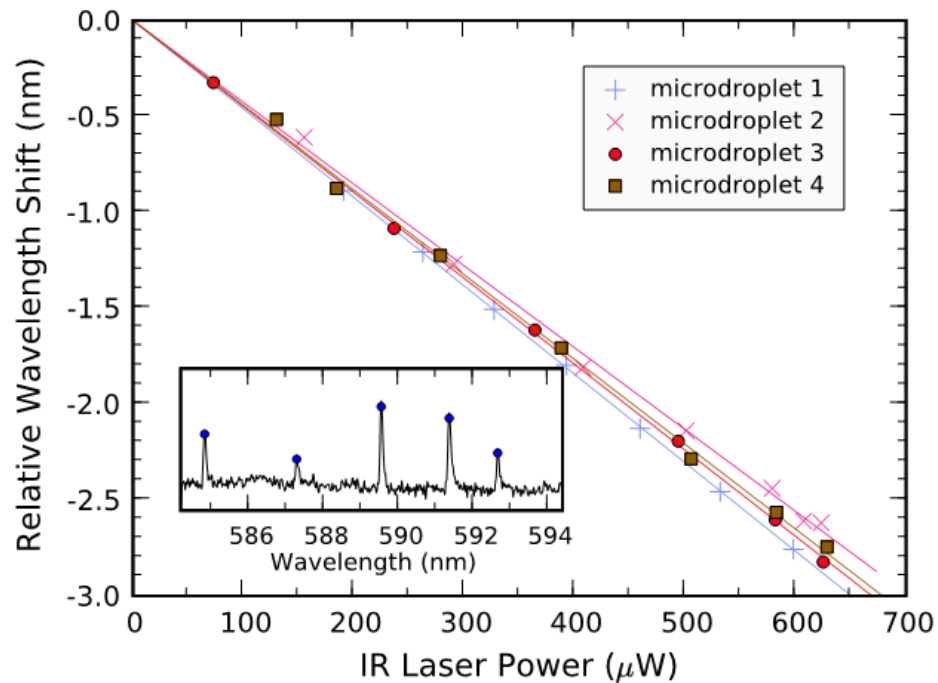

Figure 3.2: Relative WGM wavelength shift with respect to the infrared laser power for different microdroplets (diameters between 9-15 µm) at the fluorescence wavelength $\lambda f \simeq$ 590 nm. Inset shows a sample spectrum from the monochromator for microdroplet 1 used to plot one data point.

Calibration curves are observed to be very linear with slopes between −4.61 nm/mW and −4.27 nm/mW for the fluorescence wavelength $\lambda_f \simeq 590$ nm. The slope at the probe laser wavelength $\lambda p = 488$ nm is obtained by multiplying this value with the ratio λ_p/λ_f taking into account the asymptotically linear relationship between the normalized drifts in the spectral position of a WGM and the microdroplet radius $\Delta\lambda/\lambda = \Delta a/a$ [9].

The linear relationship between the spectral drift of the WGMs and the infrared laser power is verified with calculations performed using the thermodynamic model described in Chapter 2. In these calculations the infrared laser power is ramped in discrete steps in a way similar to what the stepper motor performs in our setup. The calculated spectral drifts observed in the WGMs at around 488 nm plotted in Fig. 3.3 as a function of time and infrared laser power for different integration times (See Appendix A). Calculations are time-resolved between the steps, meaning that it is not assumed that an asymptotic equilibrium is reached between each step. Despite this, the tuning curves obtained in this fashion are highly linear; furthermore, the tuning range is almost constant when the step interval is ≥ 100 ms. Since the linear curves are almost fully overlapped, they seem to be a single line in Fig. 3.3. Lower values of the step interval lead to a decreased tuning range as well as a degradation of the linearity between the relative wavelength shift and the infrared laser power. This result leads us to conclude that microdroplet tunability is continuous and linear to a very good approximation, provided that a sufficiently long integration time ($\geq$ 100 ms) elapses between consecutive stepper motor positions.

The resolution of our measurements is imposed by the precision to which we can adjust the infrared laser power. Due to the cosine shape of the power tuning curve (as shown in the inset of Fig. 3.1), this resolution is not constant across the tuning range. For the stepper motor used in our setup (3300 steps per half-turn), at the position where the rate of change of the infrared laser power is maximum (and therefore where the resolution is the lowest), the power tuning precision is 9.5×10^{-4} $\Delta\lambda_{max}$, where, $\Delta\lambda_{max}$ denotes the magnitude of the

maximum spectral drift observed for the maximum available infrared laser power. For typical values of the wavelength shift calibration measurements in our microdroplets (as in Fig. 3.2), this leads to a wavelength tuning precision of $\sim$ 0.002 nm taking into account the maximum infrared laser power of 625 µW used in our experiments. This corresponds to a spectral resolution of $\sim$ 0.004 nm, considering that three data points should be recorded to resolve a peak. Similarly, a measurement near the edge of the power tuning curve, where the rate of change of the infrared laser power is smaller, leads to a higher photothermal tuning resolution. For instance, at a phase angle of $\pi/6$ on the cosine, the power tuning precision is 4.75×10^{-4} $\Delta\lambda_{max}$ corresponding to a spectral resolution of $\sim$ 0.002 nm in our experimental conditions.

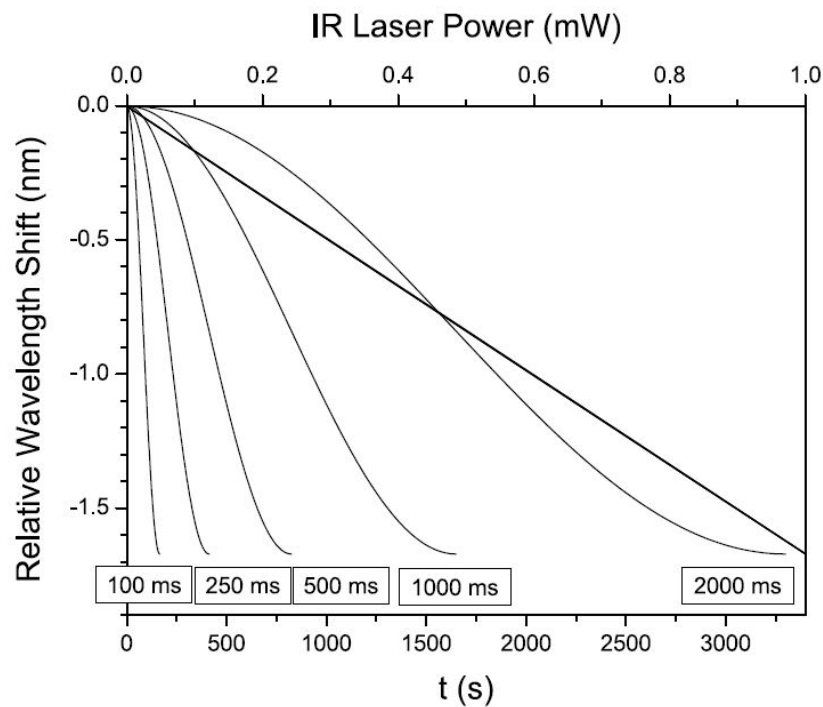
Figure 3.3. Calculated relative WGM wavelength shift from a 12 µm diameter microdroplet as a function of time and infrared laser power, considering different integration times of 100 ms, 250 ms, 500 ms, 1000 ms, and 2000 ms. The sinusoidal curves

show the relative wavelength shifts calculated as a function of time as the infrared laser power is increased as in the experiment. The linear curves show the calculated relative wavelength shift as a function of the infrared laser power using different integration times. The linear curves almost fully overlap for the selected integration times.

3.4 Results

Microdroplets with a larger contact angle were selected by visual inspection of the microscope images, especially when aiming to measure high Q-factors. The equatorial planes of these microdroplets are located higher above the surface than those of other microdroplets of similar sizes. Photothermal spectroscopy experiments performed on such microdroplets commonly revealed peaks with quality factors within the range $40000 - 100000$. Furthermore, most of the times, these peaks did not exhibit the lifting of the azimuthal degeneracy which is a characteristic of spheroid deformations of microdroplets [35]. This indicates that the associated microdroplets had good sphericity.

Figure 3.4 shows the photothermal spectra recorded from a 12 µm diameter microdroplet giving one of the highest Q-factors that we have measured ($Q \simeq 95000$ in this case), together with the associated wavelength calibration curve (Fig. 3). The photothermal spectrum shown in Fig. 4a is recorded using an integration time of 250 ms. The Lorentzian fit made to the WGM peak observed at around -0.5 nm relative wavelength shift in this spectrum reveals a FWHM of 0.0051 nm, corresponding to a Q-factor of 95000. The regular shape of the recorded peaks for this example indicates that the radius of the microdroplet is being tuned precisely between each data point on the curve; we can therefore convert the wavelength tuning precision (of the order of ~ 0.001 nm here) to a radius tuning precision of the order of $\leq 1 \text{Å}$.
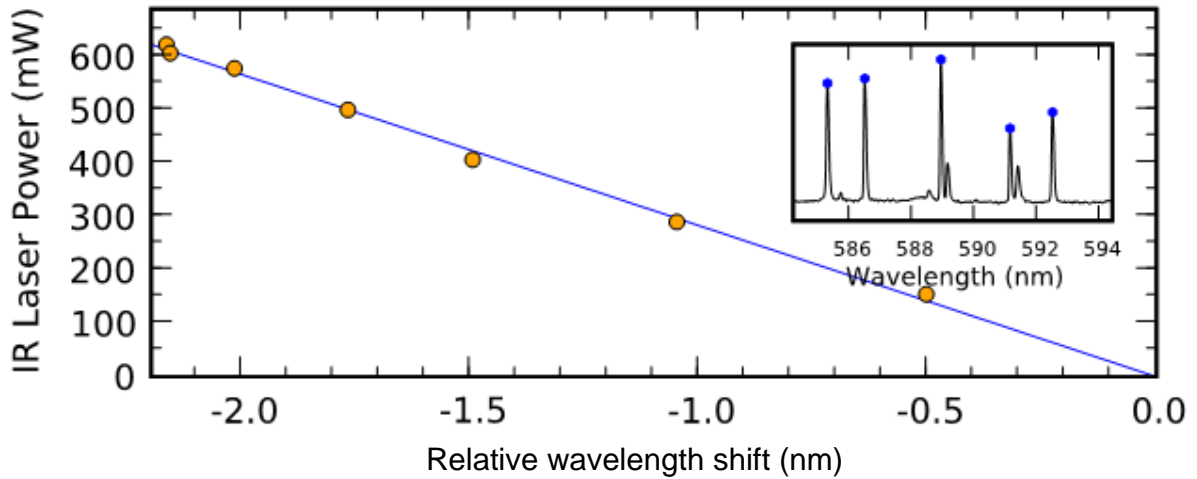
Figure 3.4. Calibration data taken from a 12 µm diameter microdroplet having a Q-factor of ~95000, showing the linear dependence of the wavelength shift on the infrared laser power, converted to the probe wavelength $\lambda = 488$ nm. Inset shows a sample spectrum from the calibration experiments. Q-factor measurements are plotted in Fig. 3.5.

The Q-factor measurement in Fig. 3.5a can in principle be affected by the fluctuations in the ambient atmosphere of the humidity chamber and by heating caused by the absorption of the blue laser. The influence of these sources of error was probed by recording two additional consecutive photothermal spectra shown in Figs. 3.5b and 3.5c with integration times of 400 ms and 500 ms, respectively. The Q-factor of the intense WGM is measured as 95000 and 98000 in Figs. 3.5b and 3.5c, which differs little from the measurement with a 100 ms integration time of Fig. 3.5a. The total time elapsed and spectral drifts observed between Figs. 3.5a – 3.5b and 3.5b – 3.5c are 290 s and 312 s, and 0.4 nm and 0.3 nm, respectively.
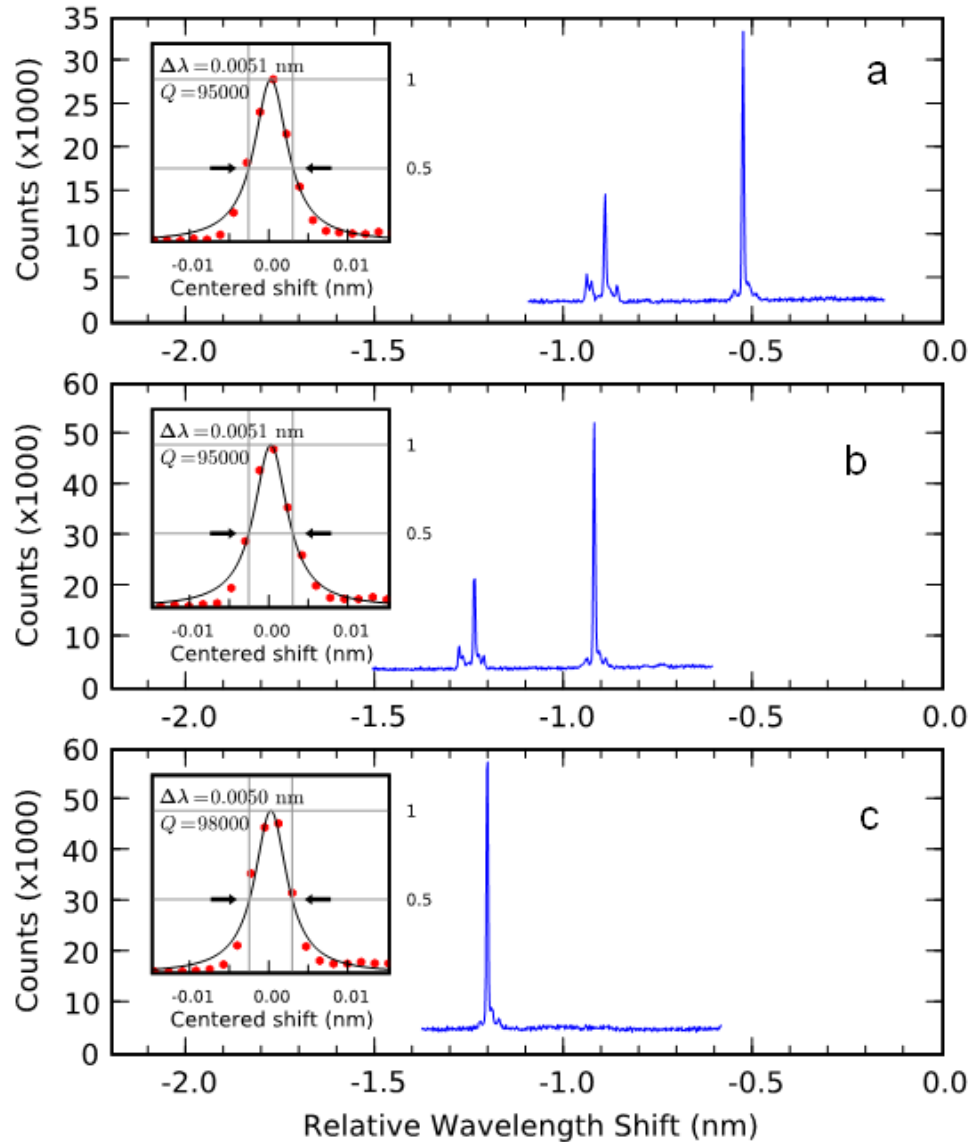
Figure 3.5. Successive spectra taken from the same (in Fig.4) 12 μm diameter microdroplet having a Q-factor of ~ 95000. The spectra in (b), (c) and (d) are taken with 250, 400 and 500 ms integration times, respectively. The observed spectral drift is attributed to the thermal instability of the chamber. Detailed view of the high-Q peak and the FWHMs are shown in the insets.

If we assume that this drift is constant during each measurement, these values imply average spectral drift rates of -0.0013 nm/s and -0.00096 nm/s, respectively. We would therefore expect spectral drifts of 0.001 nm, 0.002 nm, and 0.003 nm while scanning the central 5 data points defining the FWHM of the intense WGM peaks in Figs. 4a, 4b, and 4c, respectively. In this scenario, the direction of the observed spectral drift would impose an increase of the measured peak widths by these amounts for the corresponding exposure times. This is however not observed in this case. The spectral drift is therefore not uniform in time, and should furthermore have a low value while scanning the peak. We can assume that the observed overall drift is the result of random fluctuations in the humidity chamber whose amplitudes were low while scanning the peak, or consists in a deterministic phenomenon that takes place at other times, either before or after having scanned the peak and possibly after the end of the measurement.

We note that for different microdroplets we have observed spectral drifts of 0.1 nm-0.8 nm in different directions between consecutive experiments ∼ 300 s apart, again with little differences in the measured Q-factors for each microdroplet at different integration times. This also excludes the possibility that the drift observed is caused by large random fluctuations as their amplitude could not systematically become negligible while scanning the WGM peaks. We speculate that the sudden blocking of the infrared laser at the end of each measurement may be a cause for instabilities leading to a spectral drift of a random amplitude and direction. Some small random fluctuations in the ambient atmosphere of the chamber should nevertheless exist since a closed-loop control mechanism is not implemented in order to stabilize the conditions (especially the temperature) in the humidity chamber [36].

In the same way, the results presented in Fig. 3.5 using different integration times exclude a significant contribution of heating caused by the absorption of the blue laser to the measured Q-factors. In the regime where the absorption of the blue laser plays a role,

we would expect the Q-factors to artificially increase at larger integration times due to the heating-induced evaporation of the microdroplet. We have indeed performed experiments at different blue laser intensities for different microdroplets, and observed an increase in the measured Q-factors with the blue laser intensity. The results shown in Fig. 3.5 were performed using lower blue laser powers, in the regime where blue laser absorption did not affect the Q-factor measurements significantly. Even though most peaks have a regular shape, some exhibit an asymmetric profile, deformations at the base, or a clustering of peaks that cannot be explained by the expected free spectral range of the observed WGMs. Figure 3.6 shows some examples of such non-ideal peaks. In Fig. 3.6a, a comb of peaks is observed that shows the distinctive features of WGMs whose azimuthal degeneracy has been lifted by a deformation of the microdroplet towards a spheroid [35]. Fig. 3.6b shows what seems to be a single wide and asymmetric peak; it is conceivable that it consists of several degeneracy-lifted azimuthal modes whose wavelength separation is beneath our resolution. Figs. 3.6c and d show non-ideal peak shapes that cannot be interpreted simply. For all the microdroplets discussed in Fig. 6 no obvious deviations from a truncated spherical geometry were observed in the images recorded from the microscope viewfinder. Despite this, the WGMs observed in the corresponding photothermal spectra revealed largely asymmetric profiles that we mainly attribute to non-isotropic changes in the light path due to deformations of the microdroplets [36]. This shows the potential of this new technique in studying the geometry of microdroplets with a high resolution.

3.5 Conclusions

In conclusion, we have implemented a new technique that enables to measure directly the Q-factors of the WGMs of salt-water microdroplets that are standing on a superhydrophobic surface and kept in a humidity chamber. We measured Q-factors up to $\sim 10^5$ from the azimuthally degenerate WGM resonances. This constitutes a one order of

magnitude improvement over the conventional fluorescence spectroscopy experiments using a monochromator. In addition to demonstrating that salt-water microdroplets standing on a superhydrophobic surface host high quality WGMs, our results show that the photothermal tuning method can control the radius of a microdroplet within a precision exceeding 1 Å during the time scale of our measurements around the resonances (several seconds). Our results can pave the way for applications in cavity quantum electrodynamics, cavity optomechanics, biological sensing, and aerosol chemistry by combining the high Q-factors, tunability, and stability of salt-water microdroplets on a superhydrophobic surface.

It is worth noting that the technique presented does not rely on a tunable laser. It enables direct Q-factor measurements at any wavelength for which a fixed-frequency CW laser is available. Furthermore, the technique offers a continuous tuning range (a few nanometers) that is much larger than that of most tunable lasers. The tuning range and resolution could further be increased by using a finer stepper motor than in our current setup, which does not constitute a fundamental limitation. Previous measurements [13] have shown that photothermal tuning of microdroplets under the same conditions have a tuning range in excess of 15 nm. It is important to choose an appropriate integration time between stepper motor positions in measuring Q-factors using the photothermal spectroscopy technique. A long integration time will increase measurement errors caused by the spectral drift induced by the chamber fluctuations. Conversely, a short integration time will lead to a lower signal-to-noise ratio from the APD, as well as a degraded wavelength tuning linearity and range. Both from simulations and experimental results, we observed that integration times within 100 ms to 500 ms provide good working conditions for these measurements.

In our experiments, photothermal tuning has, by nature, a characteristic time of the same order of magnitude as the spectral drift observed in the WGMs due to environmental fluctuations in the humidity chamber. This implies that an active stabilization scheme may be implemented that would lock a WGM to an external frequency reference in a feedback
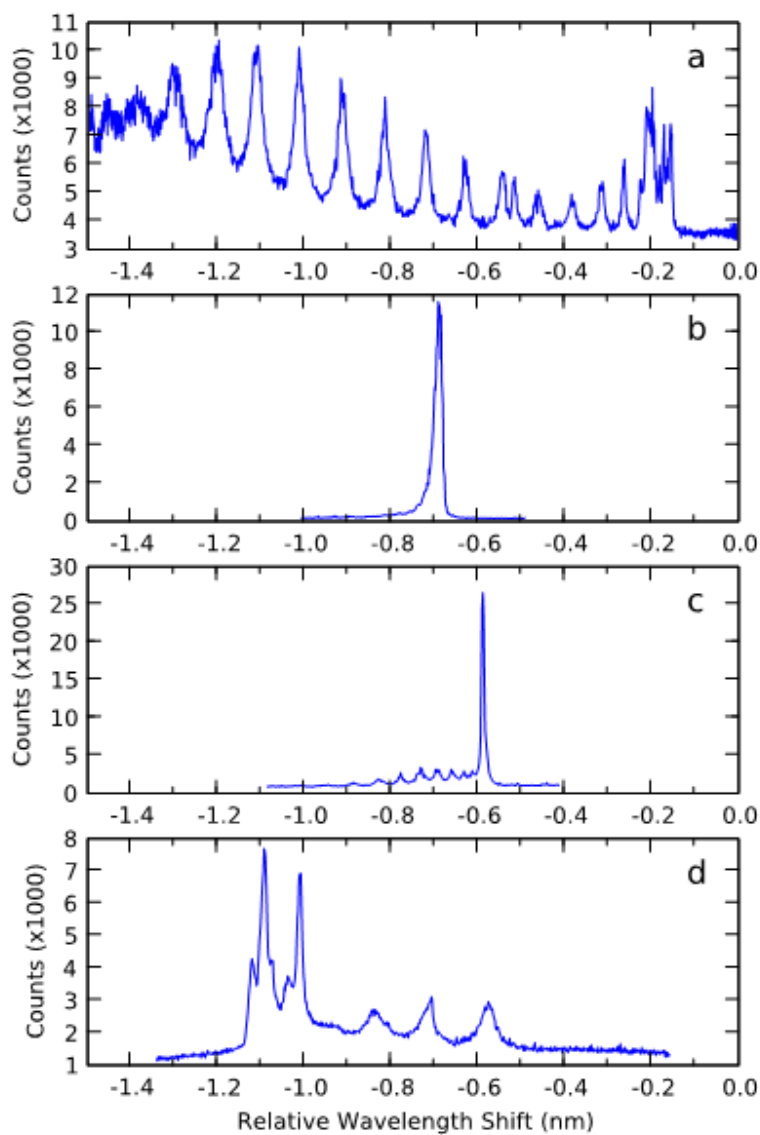
Figure 3.6. Spectra of non-ideal microdroplets. Observation of (a) the azimuthal degeneracy lifting of the WGMs, and (b) an azimuthally degenerate asymmetric low quality WGM. (c) and (d) show WGM peaks with more complicated structures. Integration times are 250 ms for a-d. Microdroplet diameters are 13 μm in a, c, d and 9.5 μm in b.

loop using the infrared laser power as the feedback actuator. In this manner, a WGM frequency could be adjusted with great freedom and then locked to a reference wavelength with the high precision demonstrated in this manuscript (≤0.002 nm). The photothermal spectroscopy technique could also be combined with a geometrical deformation of the microdroplets realized by microfabricated electrical contacts [35]. The controlled deformation of a microdroplet towards a spheroid would lift the azimuthal degeneracy of the WGMs, enabling the characterization of two-fold degenerate WGMs with higher Q-factors. A tapered optical fiber can also be used in coupling the probe laser to non-degenerate WGMs for ultrahigh Q-factor measurements using photothermal spectroscopy [25]. Such ultrahigh Q-factor measurements would also require more stable conditions in the humidity chamber, which could be achieved by implementing a closed-loop temperature control system.

We later checked the accuracy of photothermal tuning spectroscopy after acquiring a tunable red laser with a range of 632 – 637.5 nm. In these experiments Rhodamine 700 was used as a fluorescent dye since its absorption profile fits well with the operation range of the tunable laser. By using the self-stabilization mechanism which was discussed in Chapter 2, we were able to measure Q-factors in the same order of magnitude. Figure 3.7 shows one such measurement. It depicts the change in the Rhodamine 700 fluorescence intensity recorded from a self-stabilized 15 µm diameter microdroplet using the APD during rough (bottom) and fine (top) scans of the tunable laser. The droplet was kept at the self-stable operation point throughout the course of the measurement. The rough scan shows the WGM observed at around 633.4 nm. This WGM is monitored with a higher resolution with consecutive fine scans performed starting from a wavelength of 633.45 nm. During an 18 min time interval, no considerable deviation is observed in the spectral position and lineshape of the WGM. The FWHM of the WGM resonance is preserved within 0.0072–0.0075nm (corresponding to a Q-factor of ~85000), while the spectral

position is observed to drift by less than 0.004 nm. These imply stabilization of the radius of the microdroplet within <1Å during 18 min.
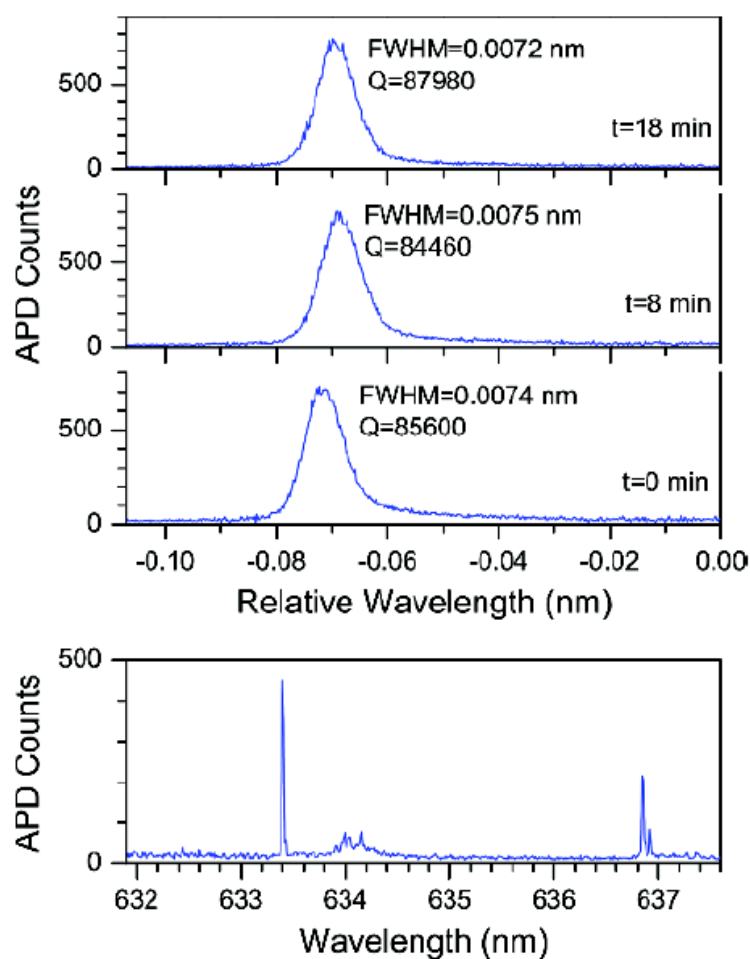
Figure 4.7. Fluorescence intensity recorded from a self-stabilized Rhodamine 700 doped 15 μm diameter microdroplet during rough (bottom) and fine (top) scans of the tunable laser, using 30 ms integration time. Initial wavelength is selected to be 633.45 nm for the fine scans. Consecutive fine scans recorded at 0, 8, and 18 min show that the quality factor of this microdroplet is ~85,000 at all times and the lineshape is well preserved. Spectral drift within 18 min is less than 0.004 nm, showing the high precision of the self-stabilization mechanism.

Chapter 4

Prolonged Raman lasing in individual salt-water microdroplets on a superhydrophobic surface

4.1 Introduction

We demonstrated in the previous chapter that liquid microdroplets can possess high-Q factor WGMs which can be utilized for practical applications. These applications include but are not limited to, photonic switching, organic light emitting device concepts, biological and chemical sensing applications and much more. Since they can be produced very easily when compared to their solid-state counterparts, microdroplets can also be used as test platforms for nonlinear optics experiments in small mode volumes.

In this sense, here, we present our studies on sustainable Raman lasing in microdroplets, which can be treated in both nonlinear optics and photonic application contexts. In fact, liquid microdroplets were among the first structures that were used in the first nonlinear optics experiments with microcavities. In those studies, liquid microdroplets were generated by a vibrating-orifice aerosol generator and they were excited with single laser pulses [37, 38]. Since then however, liquid microdroplet have not been used in photonic applications mostly due to their fragile nature against external disturbances unlike solid-state microcavities [39 – 42]. Before going further, we introduce Raman scattering and the previous situation in droplet based Raman lasers.

4.2 Raman Scattering

In its simplest form, scattering of light from a particle can be classified into three groups as *Stokes*, *anti-Stokes* and *Rayleigh scattering*s. The last one differs from the first two as the energy of the photon is conserved. In Stokes (anti-Stokes) scattering, energy of the scattered photon is lower (higher) than that of the incoming photon. Figure 4.1 depicts these three scattering types.
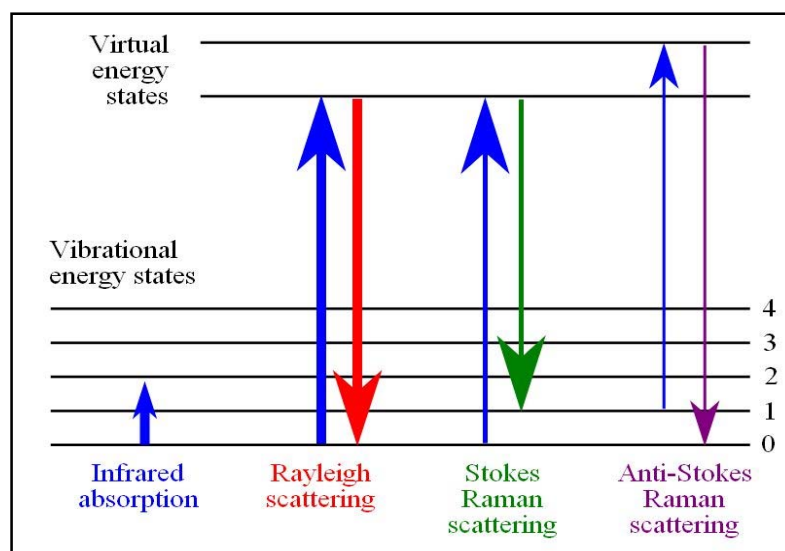
Figure 4.1. Light absorption and scattering from molecules.

Raman scattering was first observed by Sir Venkata Raman in 1923 [1]. In the above figure, energy levels 0 – 4 are real energy levels associated with the vibrational modes of a molecule. If the incoming light has higher energy than these modes, the molecule will be excited to a so-called virtual energy states which has a decay time in the order of picoseconds in contrast to the nanosecond order of magnitude in fluorescence decay times. So, the state quickly relaxes back to real energy states in three ways. In Stokes-scattering, the energy difference is released into the medium as phonons which in turn, cause

excessive heating of the medium. This will be discussed in the next sections. Raman spectra of materials are broad (see Fig. 4.3), due to high number of available transitions and fast nature of phonon relaxation.

Raman scattering in cavities are particularly interesting, since scattered light can couple to a high-Q cavity mode, which means it circulates inside a cavity in long time scales which finally give rise to peaks in specific spectral points. This is called cavity-enhanced Raman scattering (CERS) and was observed in various types of microcavities including silica microspheres [15], toroids [43] and droplets [15]. Figure 4.2 shows CERS spectrum obtained from glycerol-water microdroplet. From Fig. 4.2 it is clear that all the cavity

Figure 4.2. CERS spectrum of a 10.9 μm-diameter glycerol–water microdroplet with a 45 s exposure time. Excitation wavelength is 488 nm [11].

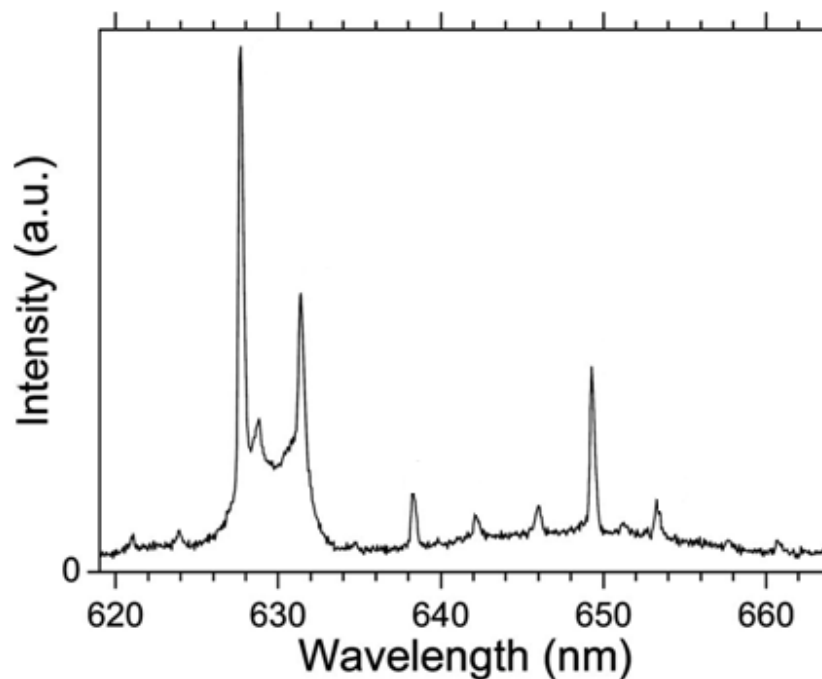modes inside the spectral gain window appear in the spectrum. If the pump power and the Q-factor of a specific cavity mode are sufficiently high, than that mode is pumped very efficiently and its intensity would get very high such that the other peaks in the spectrum are indiscernible. This situation is called Raman lasing, it is again observed in the above-mentioned cavity structures.

Recently, Raman lasing has been observed in microdroplets whose positions were stabilized using a superhydrophic surface [11] or electrodynamic levitation [44]. Achieved Raman lasing could not be sustained for long time periods due to frequent breaking of the resonance condition, which was mainly caused by thermal fluctuations induced in the liquid microdroplet during the buildup of the large WGM intensities at the Raman band.

In this chapter, we present Raman lasing from salt-water microdroplets over long time-periods. The technique we use employs two lasers: a CW infrared (IR) laser for photothermal tuning of the size [17 − 18], and a pulsed green pump laser for Raman excitation. The IR laser brings the droplet to a size in resonance with the green pump laser. At this size, the resonant absorption of green laser provides self-stabilization [12, 36, 46], which helps maintain a fixed size required for prolonged Raman lasing.

4.3 Experimental Setup

Superhydrophobic surfaces were prepared as described in Chapter 1. 3 M NaCl-water solution is sprayed onto the superhydrophobic surface by an ultrasonic nebulizer. Sample containing the microdroplets is then attached to a humidity controlled chamber with relative humidity fixed at 84.34% by a saturated KCl-water solution (KCl-W) in a small extension to the main body of the chamber as shown in Fig. 1. Temperature of the chamber is fixed at ~22 °C using a thermo-electric cooler (TEC), without any effort of temperature control. A Q-switched, frequency doubled Nd:YAG laser operating at 532 nm (repetition rate=1 kHz, pulsewidth=100 ns) is used for excitation of microdroplets. Excitation beam is

focused to a ~10 μm spot centered at the rim of microdroplets using an oil-immersion objective (NA=1.40, 60x) in the inverted geometry. Average power of the excitation beam is measured to be 8-10 mW at the focus of the objective. A CW IR laser (λ=1064 nm, maximum output power=300 mW) focused at the center of a microdroplet is used for non-resonant photothermal tuning of the size. The IR laser power (P_{IR}) is controlled using a half-waveplate (WP) rotated by a stepper motor (9200 steps/revolution) followed by a polarizing beam splitter (PBS1). A powermeter is placed at the other output of the PBS1. IR beam is combined with the excitation beam at a dichroic mirror (DM1) which directs both beams to the input port of the microscope. Raman signal is collected through the same objective, reflected off another dichroic mirror (DM2), and transmitted through a long pass filter (LP) to another polarizing beam splitter (PBS2). Signal in the reflected arm of the PBS2 is passed through a band pass filter (BP) and then detected by a photomultiplier tube (PMT) to monitor the individual Raman pulses. Signal transmitted through PBS2 is dispersed by a monochromator (spectral resolution=0.07 nm) and detected by a CCD camera with an exposure time of 50 ms.

4.4 Size stabilization

The sustained Raman lasing is made possible by using the size stabilization technique described in Chapter 2 with a slight difference. Previously described size stabilization, which was also used in Q-factor measurements, depends only on a single laser, which is the IR laser. In that scheme, IR laser is responsible for both absorption heating and resonant heating. However, in this experiment absorption heating is due to the IR laser, whereas the resonant heating required for size stabilization is due to the green pump laser. After making this distinction we proceed on describing sustained Raman lasing. Photothermal tuning allows for precise tuning of the volume of binary microdroplets by adjusting P_{IR} [10]. For the case of a salt-water microdroplet, this
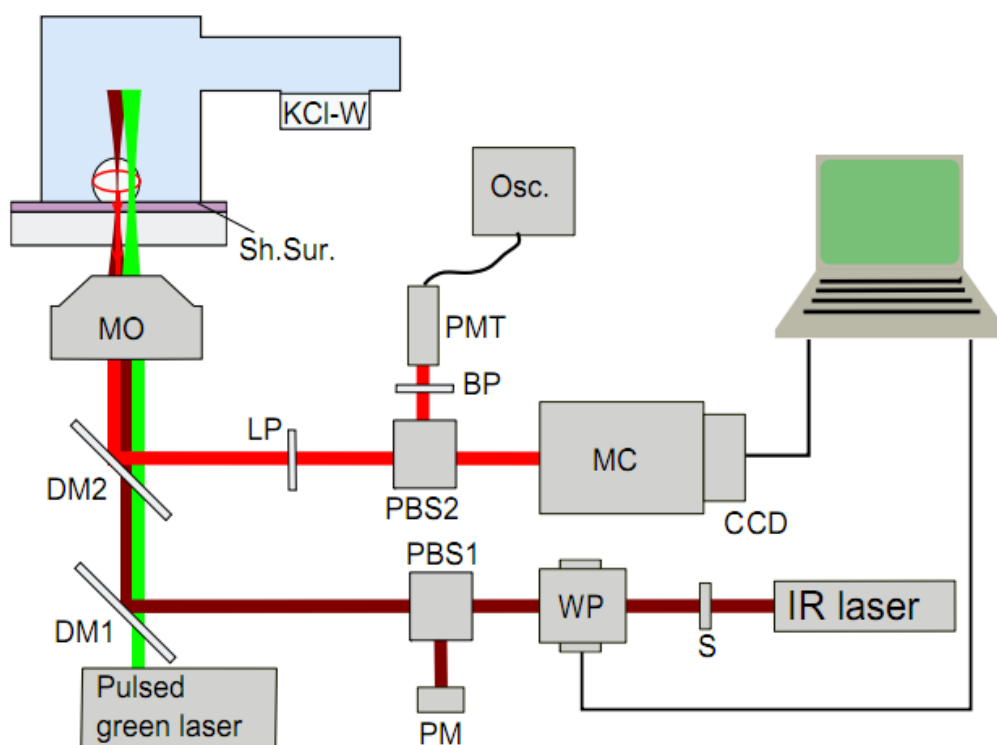
Figure. 4.3. Experimental setup. KCl-W: Saturated KCl solution, Sh. Sur: Superhydrophobic surface, MO: Microscope objective, DM: Dichroic mirror, PM: Powermeter, PBS: Polarizing beam splitter, BP: Band pass, LP: Long pass, Osc: Oscilloscope, MC: Monochromator, WP: Rotating half-waveplate, S: Shutter.
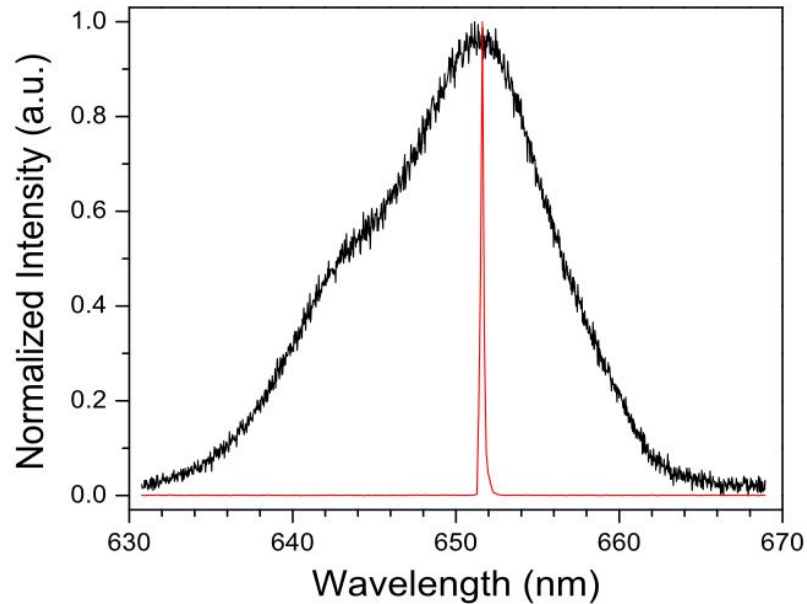
Figure 4.4. Normalized spectra of; Raman scattering of bulk 5.9 M NaCl solution (black) and Raman lasing from a microdroplet.

tuning mechanism can be almost fully reversible owing to the non-volatility of salt at room temperature [13]. Changing P_{IR} slowly ensures -to a good approximation- a one to one correspondence between this parameter and the droplet size. Figure 4.5 shows the total intensity between 627-669 nm collected from a 12 µm-diameter droplet, plotted against P_{IR}. P_{IR} is varied smoothly, following one period (period= 205 s) of a sinusoidal wave, starting from the minimum. Calibration experiments under these experimental conditions revealed a photothermal tuning range of ∼ 4 nm at the maximum P_{IR} value of 1.04 mW for WGMs near 650 nm. Being heated by the IR laser, the droplet first shrinks down to a smaller volume, and then swells back to its initial size again. Consequently, the droplet takes on a particular size twice; first during shrinking, then during swelling. These two sweeps over the accessible sizes are colored in blue and red for increasing and decreasing P_{IR}, respectively. During the sweep, the WGM resonance for the 532 nm pump light

becomes satisfied at a certain size. This results in much more efficient pumping of the Raman gain medium, giving rise to lasing. Among the sizes swept, lasing occurs at the size corresponding to a P_{IR} of 0.55 mW in the increasing-P_{IR} direction. In the decreasing-P_{IR} direction lasing occurs from 0.55 to 0.43 mW, during a larger part of the sweep. The inset compares spectra corresponding to P_{IR} of 0.55 mW and 0.49 mW recorded during the increasing and decreasing P_{IR} sweeps, respectively. As expected, the peaks in the spectra coincide exactly at 649.45 nm, indicating that lasing occurs at the same size, independent of where this size is approached from. The WGM peak remains exactly at 649.45 nm while P_{IR} is swept from 0.55 to 0.43 mW in the decreasing direction, indicating self-stabilization of the microdroplet size.
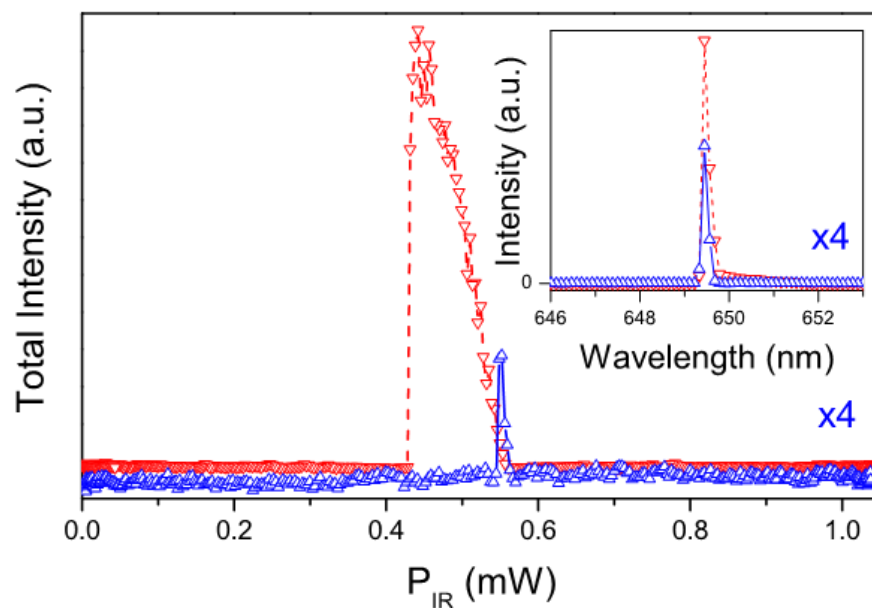

Figure 4.5. Total intensity versus infrared laser power (P_{IR}), collected from a 12 μm-diameter NaCl-water microdroplet exhibiting Raman lasing in increasing (blue solid) and decreasing (red dashed) P_{IR} sweeps. Inset shows Raman lasing spectra from increasing (blue solid) and decreasing (red dashed) P_{IR} sweeps. Intensity during increasing P_{IR} is multiplied by 4 for clarity

4.5 Results

A hysteresis is clearly seen in the P_{IR} dependence of the total Raman lasing intensity, shown in Fig. 4.5. We attribute this hysteresis to the resonant heating mechanism that occurs when a WGM absorption gets in resonance with the green laser at a definite droplet size. As the resonant size is approached from above, the evaporation rate gets accelerated by the resonant heating. This causes the droplet to pass over the resonant size too rapidly, resulting in an instantaneous lasing only. However, when the resonant size is approached from below, self-stable operation points can be found where Raman lasing can be sustained for long time periods. At such an operation point, the resonant heating resists size changes by decelerating (accelerating) the condensation rate upon an increase (decrease) in the microdroplet size. It is therefore necessary to start from a smaller size and gradually decrease P_{IR} in bringing the droplet to a self-stable operation point.

Self-stabilization requires spectral tuning over half-linewidth of the absorbing WGM at 532 nm. Assuming a quality factor of 10^4, this translates to a temperature change (ΔT) of approximately 1 mK in the microdroplet, for the relative humidity used in our experiments [13, 17]. First principle calculations assuming laser absorption through the diameter of the microdroplet [47] reveals green pump power necessary to change the microdroplet temperature by 1 mK, to be 7 mW. Laser induced temperature change of a microdroplet is given in Ref. 45 as,

$$\Delta T = \frac{aP}{2\pi K_a a}\left(1 + \frac{fQ}{2ka}\right)$$

where, P is the power of the tweezing laser, f is the fraction of the laser that is coupled to a WGM with a q-factor of Q, K_a is the thermal conductivity of the surrounding air (26.2×10^{-3} Wm^{-1} K^{-1} at 300 K), k is the wavenumber of the light, a is the radius and finally a is the absorption coefficient of water at the laser wavelength. If we assume that all Raman phonons contribute to the heating, then f should be 0 and a to be 1. In this manner, we can use this equation to calculate the heating due to Raman phonons. Plugging the remaining

terms in the equation, P is found to be ~11 nW. Although this level of green laser power is available in our experiments, heat generated during Raman conversion process should also be taken into account. Another simple calculation would give the energy of phonons associated with the Raman process. Transition takes place between 532 nm and 650 nm, which would yield energy difference of 6.87×10^{-20}J. The rate of phonon conversion is therefore found to be ~1.6×10^{11}s^{-1}. We can conclude that heating due to Raman process can also play a significant role in this resonant heating mechanism if we consider the total CCD counts detected from a WGM exhibiting Raman lasing (typically 10^6 counts/s), the low digital conversion gain used in the experiments, the overall detection efficiency of the experimental setup, and the low collection efficiency of the WGMs because of detection in the inverted geometry [17].

Figure 4.6a shows the consecutive spectra of ~25 minutes of Raman lasing recorded from a 14 μm-diameter droplet. Lasing occurs at the intense WGM peak at 651.6 nm that lies within the Raman band of water for 532 nm excitation. Recording spectra covering the whole Raman band enabled us to check if lasing occurs at other spectral locations, and as is the case with the droplet of Fig.4.6a, we mostly observed lasing at a single wavelength. The stable spectral position of the lasing wavelength shows that the droplet remained in its resonant size during the whole measurement. The maximum intensity of the consecutive spectra and the P_{IR} are plotted against time on the left and right vertical axes of Fig.4.6b, respectively. Raman lasing intensity is calculated by integrating a spectral window with a 3 nm width around the peak (See Appendix B). The sudden decrease of the P_{IR} appearing in the beginning of the acquisition is part of the sinusoidal sweep, where no lasing size has been met yet. The lasing intensity exhibits both short and long-time fluctuations. We attribute the fast fluctuations to the unnegligible heat release during Raman conversion. The longer time scale fluctuations originate from temperature variations of the chamber. In order to compensate for these variations and keep the droplet at the self-stable operation
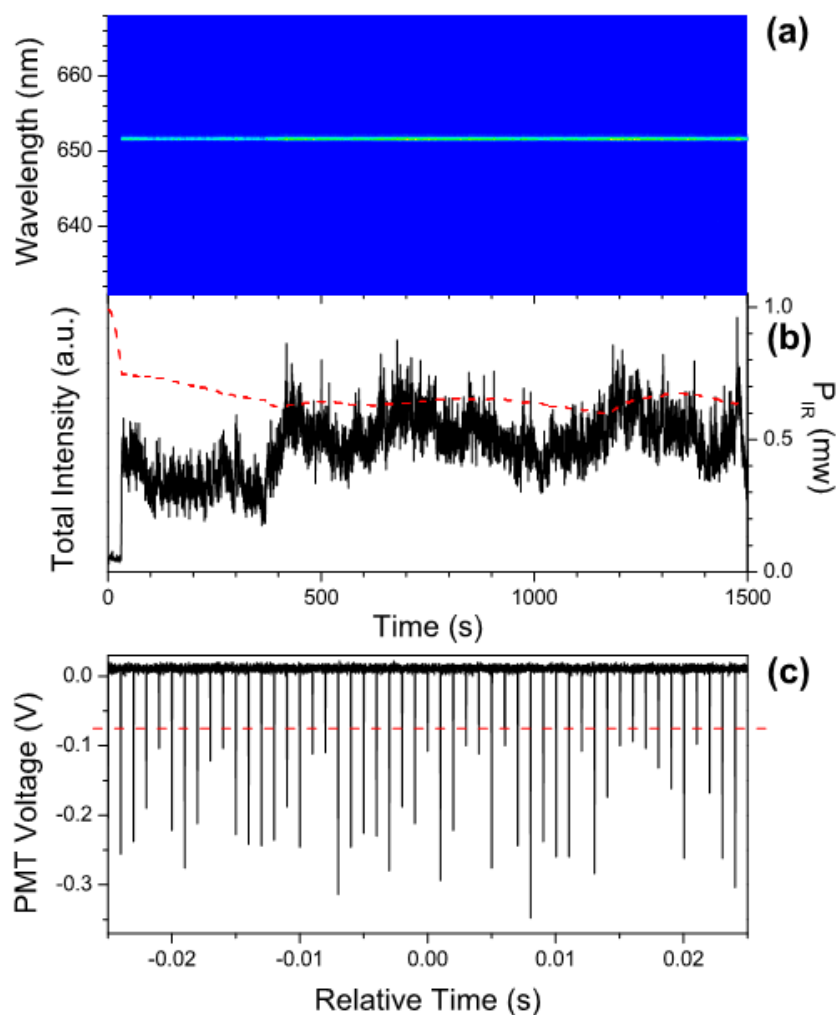
Figure 4.6. (a) Consecutive spectra showing prolonged Raman lasing from a 14 μm-diameter microdroplet. (b) Maximum intensity of each spectrum in (a) (black solid) and the power of the infrared laser (red dashed) during the lasing period. (c) Oscilloscope traces showing pulse train of Raman lasing signal. Red dashed line denotes the background level.

point, P_{IR} was adjusted manually during Raman lasing. After recording sufficient data, experiments were stopped manually by blocking the pump laser.

The output pulse train of lasing period at 1 kHz measured using an oscilloscope is shown in Fig.4.6c. The red dashed line denotes the average level of pulse train due to the residual spontaneous Raman scattering, recorded from the same microdroplet in the absence of Raman lasing. The lasing pulses are clearly distinguished from the background by their higher intensities, and they constitute 70% of the total pulses.

We demonstrated prolonged Raman lasing for durations as high as 25 minutes using the self-stabilization mechanism. Technique we present does not put any limitations on the lasing durations. The system may be more effective if the long-term fluctuations in the chamber are suppressed by activating a closed-loop feedback control thus eliminating the need for manual adjustments of the IR laser. This study may inspire novel microdroplet-based light source applications and may pave way for nonlinear optics experiments using microdroplets in a more stable manner than those of the previous experimental configurations.

Chapter 5
Conclusions

In this thesis we introduced a new method for measuring Q – factors of liquid droplets standing on a superhydrophobic surface. The method facilitates the previously demonstrated photothermal size tuning and allowed us to overcome limits of our experimental setup. Calibration experiments revealed linearity in size tuning, which also confirms previous results. We present a 10 – fold improvement in the measured Q – factors. Previous results were around 8100 whereas this method enable us to measure Q – factors as high as 10^5. We also confirmed our results after acquiring a tunable laser. Since the resolution of the tunable laser is higher than the method presented here, i.e. measured linewidths are well above the resolution of the laser, we think that inhomogeneous broadening due to degenerate azimuthal modes lead to this value. So, future work in our laboratory will focus on tapered fiber coupling to one specific azimuthal mode.

In the second part, we made use of the photothermal tuning along with the size stabilization technique to prolong the duration of Raman lasing in microdroplets. We photothermally tune the size of a droplet to a proximity of a resonance of the pulsed green laser. From then on, resonant heating of the pump laser leads to size stabilization. The method we present puts no limitations on the lasing duration so all experiments were stopped manually after we gathered enough data for analysis. We presented ~1000 time increase in the lasing duration. However, long term fluctuations affect droplets, so we manually adjusted the power of the heating laser when needed. This experiment may open way for nonlinear optics experiments in droplets. Our experimental configuration and technique have great advantage of stability since all the previous related work were done with levitated or a stream of droplets. Future focus may be on frequency comb generation or parametric conversion experiments.

Appendix A
MATLAB Program for calculating the tuning range with respect to different integration times and IR laser power

```
%%%%%%%%%%%%%%%%%%%%%%%%% Global variables
global alpha_prev qtilda_prev mol_Na_Cl
global V_A m_A m_Na_Cl R_cons Delta_HvA C_PA D_AC k_g w_0
%%%%%%%%%%%%%%%%%%%%%%%%%%


%%%%%%%%%%%%%%%%%%%%%%%%%%% Constants
V_A=18.0684e-6;                         % m^3/mol (molar volume)
m_A=18.016;                              % g/mol (molar mass)
m_Na_Cl=58.44277;                        % g/mol (molar mass)
R_cons=8.314472;                        % J/(mol*K)
Delta_HvA=43990;                        % J/mol
% Handbook of C&P p987
% C_PA=75.327;                             % J/(mol*K), for water

%cont_ang=150*pi/180;                     % rad
cont_ang=160*pi/180;                    % rad
f_theta=0.5*(0.00008957 + 0.6333*cont_ang + 0.116*cont_ang^2 - ...
    0.08878*cont_ang^3 + 0.01033*cont_ang^4);
%pause;
D_AC=f_theta*0.242e-4;                          % m^2/sec
% Tu PhD thesis p52
area1=pi*cos(cont_ang-pi/2)^2;
area2=2*pi*(1+cos(pi-cont_ang));
k_g_a=f_theta*0.02620;                          % W/(m*K), for air
k_g_bs=1.14;                            % W/(m*K), for borosilicate glass
k_g=(area1*k_g_bs+area2*k_g_a)/(area1+area2);
%%%%%%%%%%%%%%%%%%%%%%%%%%


%%%%%%%%%%%%%%%%%%%%%%%%%% File names
out_file_out1=sprintf('%s','otime.txt');
out_file_out2=sprintf('%s','oPlaser.txt');
%%%%%%%%%%%%%%%%%%%%%%%%%%


%S_A=0.7530;
%S_A=0.9730;
S_A=0.8434;
%S_B=0.12;
%S_B=0.05;


%%%%%%%%%%%%%%%%%%%%%%%%%%%%% Define and save laser power
P_min=0;                                % minimum laser power
```

```
P_max=1.0e-3;                              % maximum laser power
ndp=1650;
%ndp=15;% number of data points
%ndp=50;                                   % number of data points
%P_laser1=0:(P_max-P_min)/ndp:P_max;
steps=0:1:ndp;
P_laser1=P_max*(1-cos(steps*2*pi/(2*1650)))/2;
%P_laser2=0:(P_max-P_min)/ndp:(P_max-(P_max-P_min)/ndp);
%P_laser2=max(P_laser2)-P_laser2;
%P_laser=[P_laser1 P_laser2]';
%save(out_file_PL,'P_laser','-ASCII','-TABS')
w_0=1000e-9;                           % focal waist
%%%%%%%%%%%%%%%%%%%%%%%%%%%%%
tinitial=0;
tfinal=2000e-3;
dt=tfinal/100;
tspan=tinitial:dt:tfinal;          % time vector

T_inf=299.55;
T_d0=299.55;


wp_0=find_eq_wp(S_A,T_d0,T_inf);
x_Na_Cl0=(wp_0/m_Na_Cl) / ( (wp_0/m_Na_Cl) + ( (100-wp_0)/m_A ) );
x_A0=1-x_Na_Cl0;


%stable_rad=zeros(length(P_laser),length(a_0_v));
rad_v=[];
t_v=[];
%stable_dl=zeros(length(P_laser),length(a_0_v));
%stable_T_d=zeros(length(P_laser),length(a_0_v));


a_0=6e-6;


V_m0 = 1e-6 * ( (x_A0*m_A + x_Na_Cl0*m_Na_Cl) / density_find(wp_0) ); %
molar volume in m^3/mol


mol_m0=(4*pi/3)*(a_0^3)/V_m0;


mol_Na_Cl=x_Na_Cl0*mol_m0;
mol_A0=mol_m0-mol_Na_Cl;


%%%%%%%%%%%%%%%%%%%%%%%%%%%% Calculate the initial qtilda
alpha_prev=2*pi*a_0/1064e-9;
qtilda_prev=Find_Q_tilda_abs(alpha_prev,w_0,1064e-9);
%%%%%%%%%%%%%%%%%%%%%%%%%%%
```

```
rad_v=[];
rad_v2=[];
for running_i=2:length(P_laser1);

    vect0=[mol_A0 T_d0];
%        options = odeset('RelTol',1e-5,'AbsTol',[1e-5 1e-5]);
    options = odeset('RelTol',1e-6);
    [tmeas,res_a] = ode15s('diff_solve',tspan,vect0,options,T_inf,...
        S_A,P_laser1(running_i));
    na_v=res_a(:,1);
    radius_v=calculate_radius(na_v);
    radius_v2=radius_v(length(radius_v));
    T_d_v=res_a(:,2);
    rad_v=[rad_v; radius_v];
    rad_v2=[rad_v2; radius_v2];
    if running_i~=2
        tmeas=t_v(length(t_v))+tmeas;
    end
    t_v=[t_v; tmeas];
    mol_A0=na_v(length(na_v));
    T_d0=T_d_v(length(T_d_v));
    running_i;

end;


%stable_dl(:,a_0i)=stable_rad(:,a_0i)/stable_rad(1,a_0i);
%stable_dl(:,a_0i)=590*stable_dl(:,a_0i)-590;

%plot(P_laser,stable_dl(:,a_0i),'-x');
dl_v=488*(rad_v-a_0)/a_0;
dl_v2=488*(rad_v2-a_0)/a_0;
dl_v2=[0; dl_v2];
out1(:,1)=t_v;
out1(:,2)=dl_v;
P_laser1=P_laser1';
out2(:,1)=P_laser1;
out2(:,2)=dl_v2;

subplot(211)
plot(out1(:,1),out1(:,2));
subplot(212)
plot(out2(:,1),out2(:,2));

save(out_file_out1,'out1','-ASCII','-TABS')
save(out_file_out2,'out2','-ASCII','-TABS')
```

Appendix B
MATLAB Program for integrating the intensity of the Raman lasing peak

```
%directory=sprintf('%s','./data/');
first_part=sprintf('%s','xyz_power_time_int_traces');
%first_part_back=sprintf('%s','series_l_');
%middle_term=sprintf('%s','');
extension=sprintf('%s','.lvm');
out_file1=sprintf('%s%s%s',first_part,'_matrix','.dat');
out_file2=sprintf('%s%s%s',first_part,'_p','.dat');
out_file_pdf=sprintf('%s',first_part);
%out_file_PLE=sprintf('%s%s%s','m_PLE',first_part,extension);


%int_thresh=500;


int_tr=load(sprintf('%s%s',first_part,extension));


[tr_rows tr_col]=size(int_tr);


matrix_final=int_tr(:,3:tr_col)-sum(int_tr(1,3:43))/41;


t_i=900;
t_f=1500;



% Summation of the data points on the peak to find total intensity
for ii=1:tr_rows;
    aa=int_tr(ii,3:tr_col);
 %  good_indices=find(aa>int_thresh);
 %  int_mat(ii)=sum(aa(good_indices));
    int_mat(ii)=sum(aa);
    time_mat(ii)=int_tr(ii,2);
end;

% Create figure
figure1 = figure('XVisual',...
    '0x27 (TrueColor, depth 24, RGB mask 0xff0000 0xff00 0x00ff)',...
    'Units','centimeters','Position',[2 2 11 20]);
% Create axes
axes1 = axes('Parent',figure1,'Units','centimeters','Position',[2 11.5
7.5 5],...
    'FontSize',9);
axes2 = axes('Parent',figure1,'Units','centimeters','Position',[2 6.5 7.5
5],...
    'FontSize',9,'TickDir','out','TickLength',[0.015
0.015],'XMinorTick','on','YMinorTick','on');
```

```
axes3 = axes('Parent',figure1,'Units','centimeters','Position',[2 1.5 7.5
5],...
    'FontSiz
e',9,'TickDir','out','TickLength',[0.015
0.015],'XMinorTick','on','YMinorTick','on');
box('on');
hold('all');

xx=1:334;
surface('Parent',axes1,'ZData',matrix_final','YData',xx,'XData',...
    time_mat/1000,'CData',matrix_final','EdgeColor','none');

%shading interp;
shading flat;

plot(time_mat/1000,int_mat,'Parent',axes2)
plot(time_mat/1000,int_tr(:,1),'Parent',axes3)

set(axes1,'XTick',[],'TickDir','out','TickLength',[0.015
0.015],'XMinorTick','on','YMinorTick','on')
axis(axes1,[0 time_mat(length(time_mat))/1000 1 334])
ylabel(axes1,'Wavelength (nm)','fontsize',12);

set(axes2,'XTick',[],'TickDir','out','TickLength',[0.015
0.015],'XMinorTick','on','YMinorTick','on')
axis(axes2,[0 time_mat(length(time_mat))/1000 0 1.05*max(int_mat)])
ylabel(axes2,'Total Intensity (a.u.)','fontsize',12);

set(axes3,'TickDir','out')
axis(axes3,[0 time_mat(length(time_mat))/1000 0 1.05*max(int_tr(:,1))])
ylabel(axes3,'P (mW)','fontsize',12);
xlabel(axes3,'Time (s)','fontsize',12);

saveas(gcf,out_file_pdf,'pdf')
save(out_file1,'matrix_final','-ASCII','-TABS')
out_m1=[time_mat' int_mat'];
save(out_file2,'out_m1','-ASCII','-TABS')
```

Bibliography

[1] C. V. Raman, *Indian Journal of Physics*, **2,** 387 (1928).

[2] L. Brillouin, *Ann. Phys.* (Paris) **17,** 88 (1922).

[3] E. M. Purcell, *Phys. Rev*. **69,** 681 (1946).

[4] A. Serpengüzel *et. al*. *Opt. Lett*. **20,** 654 (1995).

[5] T.J. Kippenberg et. al. *Appl. Phys. Lett*. **83,** 797 (2003).

[6] D. K. Armani *et. al*., *Nature* **421,** 925 (2005).

[7] T. Heindel *et. al*. *Appl. Phys. Lett*. **92,** 091107 (2008).

[8] M. Bayindir *et. al*. *Phys. Rev. Lett*. **84,** 2140 (2000).

[9] H. M. Tzeng *et. al.* *Opt. Lett*. **9,** 273 (1984).

[10] A. Kiraz et. al, Appl. Phys. Lett. **89,** 081118 (2006).

[11] A. Sennaroglu et. al. *Opt. Lett*. **32,** 2197 (2007).

[12] A. Kiraz et. al., *J. Opt. Soc. Am. B* **24,** 1824 (2007).

[13] A. Kiraz *et. al. Phys. Chem. Chem. Phys*. **11**, 2597 (2009).

[14] H. Azzouz, "*Liquid droplet dye laser*", Master's thesis, Technical Universty of Denmark, (2005).

[15] M. H. Fields, *et. al*, "Nonlinear optics in microspheres," in *Progress in Optics* (E. Wolf, ed.), vol. 41, pp. 1–95, Elsevier, (2000).

[16] M. L. Gorodetsky *et. al*. Opt. Lett. **21**, 453 (1996).

[17] A. Kiraz et. al. *Proc. of SPIE* **7038**, 70381I (2008).

[18] Y. Karadağ, "*Spectral tuning of liquid microdroplets standing on a superhydrophobic surface by using a focused laser or electrowetting*" , Master's thesis, Koç University, Istanbul. (2009)

[19] K. J. Vahala, *Nature* **424**, 839 (2003).

[20] T. J. Kippenberg and K. J. Vahala, *Opt. Express* **15**, 17172 (2007).

[21] A. M. Armani, R. P. Kulkarni, S. E. Fraser, R. C. Flagan, and K. J. Vahala, *Science* 317, 783 (2007).

[22] F. Vollmer and S. Arnold, *Nature Methods* 5, 591 (2008).

[23] F. Vollmer, S. Arnold, and D. Keng, *Proc. Natl. Aca. Sci*. **105**, 20701 (2008).

[24] D.W. Vernooy, V. S. Ilchenko, H.Mabuchi, E.W. Streed, and H. J. Kimble, *Opt. Lett*. **23**, 247 (1998).

[25] D. K. Armani, T. J. Kippenberg, S. M. Spillane, and K. J. Vahala, *Nature* **421**, 925 (2003).

[26] J. P. Reid, H. Meresman, L. Mitchem, and R. Symes, *Int. Rev. Phys. Chem*. **26**, 139 (2007).

[27] A. Serpengüzel, J. C. Swindal, R. K. Chang, and W. P. Acker*, Appl. Opt*. **31**, 3543 (1992).

[28] J.-Z. Zhang, D. H. Leach, and R. K. Chang, *Opt. Lett*. **13**, 270 (1988).

[29] S. Arnold and L. M. Folan, *Opt. Lett*. **14**, 387 (1989).

[30] S. Arnold and L. M. Folan, *Rev. Sci. Inst*. **57**, 2250 (1986).

[31] A. Ashkin and J. M. Dziedzic, *Science* **187**, 1073 (1975).

[32] R. J. Hopkins, L. Mitchem, A. D. Ward, and J. P. Reid, Phys. Chem. Chem. Phys. 6, 4924 (2004).

[33] A. Kiraz, Y. Karadağ, and M. Muradoğlu, *Phys. Chem. Chem. Phys*. **10**, 6446 (2008).

[34] M. Orrit and J. Bernard, *Phys. Rev. Lett*. **65**, 2716 (1990).

[35] S. C. Yorulmaz, M. Mestre, M. Muradoglu, B. E. Alaca, and A. Kiraz, *Opt. Commun*. **282**, 3024 (2009).

[36] Y. Karadag, M. Mestre, and A. Kiraz, *Phys. Chem. Chem. Phys*. **11**, 7145 (2009).

[37]. S.-X. Qian and R. K. Chang, *Phys. Rev. Lett*. **56**, 926 (1986).

[38]. H.-B. Lin, A. L. Huston, J. D. Eversole, and A. J. Campillo, *J. Opt. Soc. Am. B* **7**, 2079 (1990).

[39]. S. M. Spillane, T. J. Kippenberg, and K. J. Vahala, *Nature* **415**, 621 (2002).

[40]. T. J. Kippenberg, S. M. Spillane, D. K. Armani, and K. J. Vahala, *Opt. Lett*. **29**, 1224 (2004).

[41]. T. J. Kippenberg, S. Spillane, and K. J. Vahala, *Phys. Rev. Lett*. **93**, 083904 (2004).

[42]. P. Del'Haye, A. Schliesser, O. Arcizet, T. Wilken, R. Holzwarth, and T. J. Kippenberg, *Nature* **450**, 1214 (2007).

[43] T. J. Kippenberg, "*Nonlinear optics in ultra-high-Q whispering-gallery optical microcavities*", PhD Thesis, California Institute of Technology, (2004)

[44]. R. Sharma, J. P. Mondia, J. Schfer, Z. H. Lu, and L. J. Wang, *J. Appl. Phys*. **105**, 113104 (2009).

[45]. M. Guillon, R. E. H. Miles, J. P. Reid, and D. McGloin, *New J. Phys*. **11**, 103041 (2009).

[46]. K. J. Knox and J. P. Reid, *J. Phys. Chem. A* **112**, 10439 (2008).

[47]. J. C. Bienfang, W. Rudolph, P. A. Roos, L. S. Meng, and J. L. Carlsten, *J. Opt. Soc. Am. B* **19**, 1318 (2002)

VITA

Mustafa Gündoğan was born in İstanbul in 1986. He was admitted to Bilkent University Physics Department after graduating from Ankara Süleyman Demirel Anatolian High School in 2004. He received the B.Sc. degree in 2008 and moved to Koç University to pursue master's studies on optical spectroscopy of liquid microdroplets. He obtained the M.Sc. degree in 2010. He will pursue his Ph.D. studies on *Solid-State Quantum Memories for Single Photons* at the Institute of Photonic Sciences (ICFO) in Barcelona, Spain as an ICFO Fellow.

LIST OF PUBLICATIONS

1. Prolonged Raman lasing in size-stabilized salt-water microdroplets on a superhydrophobic surface Y. Karadag, <u>M. Gündoğan</u>, M. Y. Yuce, H. Cankaya, A. Sennaroglu, and A. Kiraz *Opt. Lett.* **35** (12), 1995-1997 (2010)

2. Photothermal Tuning and Size Locking of Salt-Water Microdroplets on a Superhydrophobic Surface M. Mestre, Y. Karadag, S. C. Yorulmaz, <u>M. Gündoğan</u>, and A. Kiraz *Int. J. Optomechatronics* **3** (4), 303-318 (2009).